1 **Explaining globally inhomogeneous future changes in monsoons using simple moist energy**

2 **diagnostics**

3

4 Rodrigo J. Bombardi [1] and William R. Boos [2,3]

5

6 [1] Department of Geography, Texas A&M University, College Station, Texas

7 [2] Department of Earth and Planetary Science, University of California, Berkeley, California

8 [3] Climate and Ecosystem Sciences Division, Lawrence Berkeley National Laboratory, Berkeley,

9 California

10

11

12

13

14

15

16

17 Corresponding author address:

18 Rodrigo J. Bombardi

19 E-mail: rjbombardi@tamu.edu

20 Department of Geography

21 College of Geosciences, Texas A&M University

22 3147 TAMU, College Station, TX, 77843, USA

23

Abstract

24

25 This study examines the annual cycle of monsoon precipitation simulated by models from the

26 Coupled Model Intercomparison Project phase 6 (CMIP6), then uses moist energy diagnostics to

27 explain globally inhomogeneous projected future changes. Rainy season characteristics are

28 quantified using a consistent method across the globe. Model bias is shown to include rainy

29 season onsets tens of days later than observed in some monsoon regions (India, Australia, and

30 North America) and overly large summer precipitation in others (North America, South America,

31 and southern Africa). Projected next-century changes include rainy season lengthening in the two

32 largest Northern Hemisphere monsoon regions (South Asia and central Sahel) and shortening in

33 the two largest Southern Hemisphere regions (South America and southern Africa). Changes in

34 the North American and Australian monsoons are less coherent across models. To understand

35 these changes, relative moist static energy (MSE) is defined as the difference between local and

36 tropical-mean surface air MSE. Future changes in relative MSE in each region correlate well

37 with onset and demise date changes. Furthermore, Southern Hemisphere regions projected to

38 undergo rainy season shortening are spanned by an increasing equator-to-pole MSE gradient,

39 suggesting their rainfall will be increasingly inhibited by fluxes of dry extratropical air; Northern

40 Hemisphere regions with projected lengthening of rainy seasons undergo little change in equator-

41 to-pole MSE gradient. Thus, although model biases raise questions on the reliability of some

42 projections, these results suggest that globally inhomogeneous future changes in monsoon timing

43 may be understood through simple measures of surface air MSE.

44

45 Keywords: monsoon, rainy season, CMIP6, SSP3-7.0, SSP5-8.5, moist static energy

46 **1. Introduction**

2

47   Monsoon systems and their variability greatly influence a large fraction of the global

48   human population. Variations in the timing of the start and end of the monsoon season and in

49   seasonal precipitation totals have important consequences for energy generation, agriculture,

50   human health, and property loss (e.g. due to landslides, floods, and fires). Thorough assessment

51   of future projections of the annual cycle of monsoon precipitation is thus of great consequence.

52   However, the effort to reliably project future monsoon rainfall has been hindered by

53   model bias, incomplete understanding of the mechanisms governing future changes, and the use

54   of disparate methodologies. Here we touch on all of these issues through analysis of the

55   historical and future seasonal cycle of monsoon precipitation simulated by the Coupled Model

56   Intercomparison Project phase 6 (CMIP6). We assess the characteristics of the wet season (e.g.

57   timing and total wet season precipitation) in core monsoon regions using a consistent approach

58   over all regions, then use simple moist energy diagnostics to frame a hypothesis for the spatial

59   inhomogeneity of the projected changes. Mechanistic hypotheses are important in such

60   assessments because of the substantial biases in model simulations of monsoons, which we also

61   examine and which have persisted since the beginning of the CMIP exercise, as documented by

62   Lambert and Boer (2001).

63   Although model biases have persisted since Lambert and Boer (2001), the representation

64   of seasonal precipitation in climate models has shown some improvement over the last two

65   decades. Several studies reported slight improvements in climate models' representation of

66   precipitation over monsoonal regions from CMIP phase 3 (CMIP3) to phase 5 (CMIP5)

67   (Monerie et al. 2012; Brown et al. 2013; Rienecker et al. 2012; Joetzjer et al. 2013; Sheffield et

68   al. 2013; Seo et al. 2013; Sperber et al. 2013; Grose et al. 2014; Lee and Wang 2014; Gulizia and

69   Camilloni 2015; Kusunoki and Arakawa 2015). CMIP5 models showed slight improvements

3

70   over CMIP3 models in simulating the observed climatological spatial and temporal precipitation

71   patterns, the seasonal evolution of precipitation, precipitation extremes, the orientation of

72   convergence zones, precipitation maxima in the vicinity of steep orography, and global monsoon

73   domain and precipitation intensity (Seo et al. 2013; Sperber et al. 2013; Lee and Wang 2014;

74   Gulizia and Camilloni 2015; Kusunoki and Arakawa 2015). CMIP5 models also showed

75   improvements in the representation of the interannual variability of tropical precipitation (Seo et

76   al. 2013; Joetzjer et al. 2013), which is associated with improvements in the representation of the

77   El Niño-Southern Oscillation (ENSO) and teleconnection patterns (e.g. Joetzjer et al. 2013).

78   Recent studies show that models participating in CMIP6 have improved representations of

79   tropical precipitation over the ocean (Tian and Dong 2020), the Indian monsoon (e.g. Gusain et

80   al. 2020), and the East Asian monsoon (e.g. Xin et al. 2020) in comparison to CMIP5 and

81   CMIP3.

82   However, other aspects of precipitation associated with monsoons remain poorly

83   represented in current climate models. Some examples are: the double ITCZ problem persists (Li

84   and Xie 2014; Oueslati and Bellon 2015; Zhang et al. 2015; Tian and Dong 2020; Fiedler et al.

85   2020); the onset of the Indian monsoon is simulated too late (Sperber et al. 2013); summer

86   monsoon precipitation over India and east Asia are underestimated (Sperber et al. 2013; Sooraj et

87   al. 2015); precipitation over the Amazon basin is underestimated (Vera et al. 2006; Bombardi

88   and Carvalho 2009; Yin et al. 2013; Gulizia and Camilloni 2015); and precipitation is

89   underestimated along (sometimes incorrectly oriented) convergence zones such as the SPCZ

90   (Brown et al. 2013; Grose et al. 2014; Niznik et al. 2015), the South Atlantic Convergence Zone

91   (SACZ, Vera et al. 2006), and the Meiyu-Baiu Front (Song and Zhou 2014).

4

92   In terms of projections for the end of the 21st century, some studies suggest that the

93   global monsoon domain will expand (Hsu et al. 2013; Huo-Po and Jian-Qi 2013; Lee and Wang

94   2014; Wang et al. 2020b), although most of the expansion is expected to occur over the ocean

95   (Lee and Wang 2014; Wang et al. 2020b), with some expansion over land in Asia (Qing 2012;

96   Lee and Wang 2014). A projected increase in precipitation over Asia is present in CMIP3 (e.g.

97   Fan et al. 2012), CMIP5 (Qing 2012; Jiang and Tian 2013; Jourdain et al. 2013; Menon et al.

98   2013; Sharmila et al. 2015; Li et al. 2015), and CMIP6 (e.g. Ha et al. 2020; Wang et al. 2020b)

99   simulations. CMIP6 models project an increase in summer rainfall (Chen et al. 2020; He et al.

100   2020; Jin et al. 2020), wet season precipitation, wet season duration, and extreme precipitation

101   over the Indian and East Asian monsoon regions (Ha et al. 2020; Moon and Ha 2020). CMIP5

102   models also project an increase in precipitation over Papua-New Guinea in the 21st century

103   (Jourdain et al. 2013). In contrast, there is no agreement between CMIP5 models regarding

104   changes in monsoon rainfall over Indonesia and Malaysia (Jourdain et al. 2013). Narsey et al.

105   (2020) also found no agreement between CMIP6 models regarding the magnitude or direction of

106   changes in precipitation over Northern Australia.

107   Global models have problems simulating the North American monsoon, with large errors

108   in their representation of the mean annual cycle and the timing of the wet season (Geil et al.

109   2013; Sheffield et al. 2013). Future projections for the North American monsoon are inconsistent

110   among models (Maloney et al. 2014). Geil et al. (2013) found that models tend to generate an

111   unrealistic flux of low-level moisture from the tropics into the North American monsoon region,

112   with a timing that unrealistically extends the monsoon season. Precipitation over the core South

113   American monsoon region (the southern Amazon and central Brazil) is well represented by

114   CMIP3 and CMIP5 models, including the seasonal cycle and interannual variability of

115   precipitation (Vera et al. 2006; Vera and Silvestri 2009; Bombardi and Carvalho 2008, 2009;

116   Jones and Carvalho 2013). Future projections indicate a southward shift of the SACZ, a delay in

117   the onset of the South American monsoon (Seth et al. 2010, 2013), and a decrease in

118   precipitation during the wet season over the core region of the South American monsoon

119   (Bombardi and Carvalho 2009; Chen et al. 2020; He et al. 2020). Future projections also indicate

120   an increase in precipitation over southern Brazil, Uruguay, and northern Argentina (Jones and

121   Carvalho 2013; Chen et al. 2020).

122   Over Africa, future projections suggest a delay of the onset of the wet season over West

123   Africa, an increase in precipitation over the central-eastern Sahel, and a decrease in precipitation

124   over the western Sahel (Monerie et al. 2012; Biasutti 2013; Roehrig et al. 2013; Chen et al.

125   2020). However, the lack of observational data in some regions makes it difficult to evaluate the

126   models' representation of precipitation and their projections for future climate change, such as in

127   the Congo region (Creese and Washington 2018). In addition, there are large differences in the

128   models' representation of African monsoons and among the models' responses to climatic

129   forcings (Biasutti 2013; Roehrig et al. 2013; Gaetani et al. 2017; Creese and Washington 2018;

130   Chen et al. 2020).

131   Understanding future changes in monsoons, and thereby obtaining greater confidence in

132   model projections, has been facilitated by various moist energy frameworks. Some of these

133   employ the vertically integrated atmospheric moist static energy (MSE) budget, in which latent

134   heating does not appear explicitly and large-scale flow can be seen as being forced by net energy

135   fluxes through the top and bottom of the atmosphere (Neelin and Held 1987). Some vertically

136   integrated energy budget frameworks can be used to causally relate changes in tropical

137   circulations to high-latitude energy source anomalies, because the anomalous meridional energy

6

138   flux needed to balance such high-latitude forcings is accomplished by quasi-diffusive eddy

139   fluxes in the extratropics but by time-mean Hadley and monsoon flow in the tropics (e.g., Kang

140   et al. 2008).

141   Other related frameworks do not leverage the MSE budget, but assume that precipitating

142   convection acts on time scales that are fast compared to those of the large-scale flow of interest

143   (e.g. seasonal monsoon circulations), yielding fluctuations of free-tropospheric temperature that

144   are in quasi-equilibrium with fluctuations in near-surface MSE (Arakawa and Schubert 1974;

145   Emanuel et al. 1994). Idealized models built on this convective quasi-equilibrium (CQE)

146   assumption were used to show how zonal advection of extratropical dry air into monsoon regions

147   limits the spatial extent of monsoon precipitation (Chou and Neelin 2001; Chou et al. 2001;

148   Chou and Neelin 2003); this "ventilation" of the high-MSE tropical boundary layer by low-MSE

149   extratropical air reduces the ability of the tropical region to convect. Related reasoning is

150   employed in the "upped-ante" mechanism, in which the free-tropospheric temperature increases

151   that occur in a warming world require larger near-surface MSE to achieve convective instability.

152   When applied temporally to the seasonal cycle, this upped-ante mechanism was invoked to

153   explain the delay in monsoon onset seen in some model simulations of future monsoons (Biasutti

154   and Sobel 2009; Seth et al. 2011; Cook and Seager 2013). This delay in monsoon onset has also

155   been referred to as an enhanced convective barrier, but it seems to only operate in simulations of

156   some future monsoon regions (e.g. North America and West Africa) and not in others (e.g. South

157   Asia), perhaps due to compensating increases in near-surface MSE (Seth et al. 2011). One of our

158   goals here is to apply some of these ideas to the CMIP6 projections, and we find that changes in

159   local near-surface MSE, perhaps caused by meridional energy fluxes, may be just as important as

160   future enhancement or reduction of any convective barrier. We also present a new metric—the

161 "relative MSE"—as a simple quantification of the the lower- and upper-level influences on

162 convective stability and an extension of the influential idea of "relative sea surface temperature"

163 (Vecchi and Soden 2007).

164 This study is organized as follows. Section 2 presents the data and methods used to

165 characterize the rainy season over monsoonal regions. Analyses of seasonal precipitation for

166 present and future climate are presented in Section 3. Section 4 shows an examination of the

167 characteristics of the wet season in historical and future scenario runs. Section 5 provides some

168 insights in the mechanism associated with changes in monsoon rainfall due to climate change.

169 The main conclusions are presented in Section 6.

170

171 **2. Data and Methods**

172 We used observed gridded precipitation data from the Global Precipitation Climatology

173 Project (GPCP, pentads, global coverage at 2.5° spatial resolution, 1980–2016, Xie et al. 2003,

174 Adler et al. 2003), the Climate Hazards group InfraRed Precipitation with Station data (CHIRPS,

175 pentads, 50°S–50°N coverage at 0.05° spatial resolution, 1981–2016, Funk et al. 2015), and the

176 Tropical Rainfall Measuring Mission (TRMM, 3B42, 50°S–50°N coverage at 0.25° spatial

177 resolution, 1998–2015, Huffman et al. 2007). In addition, we used 2-meter temperature, 2-meter

178 dewpoint, and surface geopotential from the fifth generation of European Centre for Medium-

179 Range Weather Forecasts (ECMWF) reanalysis (ERA5, daily, global coverage at 0.75°

180 horizontal spatial resolution, 1981–2010, Hersbach et al. 2020).

181 We also used daily precipitation, 2-meter temperature, and 2-meter specific humidity, and

182 topography from 12 models participating in CMIP6. Three different scenarios were considered:

183 historical runs and future scenarios represented by Shared Socio-Economic Pathways (SSPs) 3-

8

184 7.0 (hereafter SSP3.70) and 5-8.5 (hereafter SSP5.85). The SSP5.85 scenario represents the

185 upper range of forcings for future scenarios, corresponding to the CMIP5 RCP8.5 scenario.

186 SSP3.70 represents a more moderate future forcing scenario (Abram, N. et al. 2019; Kriegler et

187 al. 2017; Riahi et al. 2017). Table 1 shows details of models considered in this study.

188   We calculated the characteristics of the rainy and dry seasons (RADS; the characteristics

189 are onset and demise dates, duration, and total precipitation during wet and dry seasons) at each

190 grid point following the methodology described in Bombardi et al. (2019), which uses only

191 precipitation data and is based on the methodology originally proposed by Liebmann and

192 Marengo (2001). For each year, precipitation anomalies are created by simply subtracting the

193 climatological annual mean precipitation from the precipitation at each time, yielding a time

194 series of anomalies at each grid point. Starting from the date of the minimum in the first seasonal

195 harmonic of the climatological mean annual cycle, which falls within the dry season for

196 monsoon regions, we calculate cumulative precipitation anomalies in time. The cumulative

197 precipitation anomaly for any given day is simply the sum of all precipitation anomalies from the

198 start date up to that same day. First, the onset of the rainy season is defined as the minimum

199 value in the time series of cumulative precipitation anomalies. Then, a quality control test is

200 applied to identify false onsets: for outliers, defined as years with onset dates outside 1.5 times

201 the interquartile range, the onset is defined as the first date of the persistent change of sign of the

202 first derivative of the smoothed time series of cumulative precipitation anomalies. Finally, the

203 dataset is checked again for false onsets and any false onset is removed and flagged as missing

204 data. The calculation of the demise date of the rainy season is calculated in the same way but

205 backwards (i.e. going back in time). Once the onset and demise dates are calculated, we calculate

206 the duration of the dry and wet seasons and the accumulated precipitation during those seasons.

9

207   To calculate the characteristics of the rainy season for CMIP6 simulations we first

208   calculated the climatological annual precipitation for each model from the historical experiment

209   (from the ensemble mean for models with multiple realizations). Then, we calculated the

210   characteristics of the rainy seasons for each realization (member) of each model (using their

211   respective climatologies) in both the historical and scenario runs. Therefore, the parameters used

212   to calculate the characteristics of the rainy season for scenario runs use the same climatological

213   values used in the historical runs. We used the same climatological parameters for historical and

214   scenario experiments to ensure the characteristics of the rainy season can be easily compared

215   between experiments; i.e. we used the same baseline for each model. If multiple realizations are

216   available for a single model, we first calculate statistics (e.g. mean, median, and interquartile

217   range) for all realizations of that model before calculating multi-model ensemble (MME)

218   statistics. Therefore, each model has the same weight in the MME statistics in any analyses

219   reported here.

220   We also mask regions where the explained variance of the first harmonic of the mean

221   annual cycle of precipitation is lower than that of the second or third harmonics. These regions

222   experience low seasonality or complex precipitation regimes (2 or 3 rainy seasons per year).

223   More details about the method can be found in Bombardi et al. (2019) and at the dataset website:

224   https://climatology.tamu.edu/research/Rainy-and-Dry-Season-RADS.html. The advantage of

225   masking these regions is that we remove from our analyses regions where the models have

226   known deficiencies, such as poor representation of the annual cycle of precipitation or too wide

227   ITCZs (e.g. Kim et al. 2008; Bombardi and Carvalho 2009). Therefore, we focus on regions with

228   well-defined wet and dry seasons in observations and simulations.

229

3. Precipitation seasonal cycle

We first evaluate the models' errors and biases in representing seasonal precipitation over low-latitude regions. Figure 1 presents the observed (GPCP) mean precipitation for the extended boreal (June-September [JJAS]) and austral summer (November-February [NDJF]) and the MME bias and the MME root mean square error (RMSE). We use the number of models that have the same sign bias as an indication of agreement among models. The models overestimate precipitation over large parts of the tropical oceans, with exceptions over the eastern Indian Ocean, equatorial Pacific, and eastern North Atlantic, where precipitation is underestimated. These results indicate model deficiencies in representing convergence zones such as the Meiyu-Baiu Front (Fig. 1C), the SPCZ, and the SACZ (Fig. 1D). Many model deficiencies regarding tropical precipitation seem to be related to representation of the intensity, extent, and position of the ITCZ (Fig. 1C,D). The double ITCZ problem is still evident (Fig. 1D). Moreover, there is a remarkable agreement among models regarding the sign of precipitation biases, with more than 80% of models showing the same sign bias over most tropical and subtropical regions (Fig. 1C-D). The biases shown in Fig. 1 have been reported in CMIP3 and CMIP5 models (Vera et al. 2006; Kim et al. 2008; Bombardi and Carvalho 2009; Sperber et al. 2013; Yin et al. 2013; Grose et al. 2014; Song and Zhou 2014; Gulizia and Camilloni 2015; Sooraj et al. 2015) and in recent studies of CMIP6 (Tian and Dong 2020; Fiedler et al. 2020).

The global monsoon domain is commonly defined as the area where summer precipitation exceeds winter precipitation by a threshold of 2 to 2.5 mm.d^{-1} and summer precipitation exceeds 55% of annual precipitation (e.g. Hsu et al. 2013; Huo-Po and Jian-Qi 2013; Lee and Wang 2014). However, this definition inherently includes transition areas between monsoonal and non-monsoonal regimes. In this study we focus on core monsoonal regions,

11

253   defined as regions where more than 80% of annual precipitation falls during the wet season (Fig.

254   2A). These regions include: central South America (similar to domains used in Seth et al., 2010),

255   the Sahel region (similar to domain used in Biasutti, 2013, but focusing on the central Sahel),

256   central southern Africa, India (commonly used domain for central India), and northern Australia

257   (similar domain used in Narsey et al. 2020). Over subtropical monsoon regions such as North

258   America (same domain used in Cook and Seager, 2013) the percentage of rain that falls during

259   the wet season is lower in comparison to tropical monsoonal regions, but it still exceeds 70%. In

260   most core monsoon regions, the models represent well the spatial pattern of the percentage of

261   annual precipitation that falls during the wet season. The largest biases are over subtropical

262   regions such as western China and the North American monsoon region, in addition to northern

263   Australia (Fig. 2B).

264   Figures 3 and 4 show the mean annual cycle of precipitation for observations and

265   simulations over the regions of interest defined in Fig. 2. The models tend to simulate too much

266   precipitation, compared to observations, during the whole year over the North American domain

267   (Fig. 3A) with evident problems representing the onset and demise of the wet season. This is

268   consistent with biases in CMIP3 and CMIP5 (e.g. Geil et al. 2013). Historical runs simulate the

269   beginning of the wet season over the Sahel earlier than observed (Fig. 3B) and the beginning of

270   the Indian monsoon later than observed (Fig. 3C), which is similar to CMIP5 simulations (Sooraj

271   et al. 2015). The models also overestimate precipitation during the peak of the wet season over

272   South America (Fig. 3D) and southern Africa (Fig. 3E), consistent with CMIP3 (Bombardi and

273   Carvalho 2009). The mean annual cycle of precipitation over northern Australia shows a delay in

274   historical runs relative to observations, where CHIRPS also show a negative bias in relation to

275   GPCP and TRMM during the wet season (Fig. 3F). These results are consistent with the dry

276 biases during local summer over the Sahel, India, and northern Australia (Fig. 1C,D) and wet

277 biases over southern Africa and southeastern Brazil (Fig. 1D).

278   Turning to the future projections, SSP5.85 simulations suggest a decrease in peak

279 monsoon rainfall and a temporal contraction of the rainy season over North America (Fig. 4A),

280 and an increase in rainfall toward the end of the wet season with a delayed demise over the Sahel

281 (Fig. 4B). Over India, SSP5.85 runs indicate an increase in peak monsoon rainfall as well as later

282 demise dates (Fig. 4C). Over the remaining regions, SSP5.85 runs show smaller changes in the

283 mean annual cycle of precipitation in comparison to historical runs (Fig. 4D-F), but with a later

284 onset and earlier demise over both South America and southern Africa (Fig. 4D,E), and small

285 changes to onset and demise over northern Australia (Fig. 4F). SSP3.70 runs show similar results

286 (not shown).

287

288 **4. Characteristics of the Wet Season in Present and Future Climate Simulations**

289   In this section we analyze in more detail how well models simulate the characteristics of

290 the rainy season (i.e. accumulated precipitation during the wet season and onset and demise

291 dates) and their projections for future climate scenarios.

292   Figures 5 and 6 present boxplots showing interannual variability of the characteristics of

293 the rainy season. These analyses used only one simulation from each model, to avoid biasing the

294 results toward models with multiple realizations. The boxplots were created by taking one value

295 (the median over the core region) for each year for each dataset. For simulations, we take one

296 value (the median) for each year for each model for each experiment. We also present boxplots

297 of anomalous values of onset and demise dates calculated using median GPCP values as the

298 reference, even for simulations.

13

299   If we compare the median values of observations and historical runs in Figures 5 and 6,

300   the results are consistent with the findings presented in Figures 3 and 4. The simulations show a

301   much larger range, due to the combination of intermodel scatter and interannual variability

302   within each model (Figs. 5,6). It is worth mentioning that CHIRPS show very homogeneous

303   values for demise dates over the Sahel (Fig. 5E), which suggests that the interannual variability

304   of demise in that region is not well represented in CHIRPS. The range in historical and scenario

305   simulations are often similar (Fig. 5,6) and the most evident differences are consistent with the

306   results from Fig. 4. For example, scenario runs show a clear shift toward later demises over the

307   Sahel (Fig. 5E) and later onsets over South America and southern Africa (Fig. 6A,D), associated

308   with increased wet season rainfall in the Sahel (Fig. 5F) and lower wet season rainfall in South

309   America and southern Africa (Fig. 6C,F). Scenario runs also show a shift toward a wetter Indian

310   monsoon (Fig. 5I).

311   The differences between future scenario SSP5.85 and historical runs suggest a delay of

312   the onset date over most of the southern hemisphere monsoon regions, in addition to tropical

313   North America, far western Africa, and southeast Asia under that climate change scenario (Fig.

314   7A). Earlier onset dates are simulated over the central and eastern Sahel and India. The future

315   scenario suggests that the wet season will end later over west Africa and the Sahel, much of

316   Mexico, and parts of southern and east Asia (Fig. 7B). Earlier demise dates are expected over

317   most southern hemisphere monsoon regions. Consistent with the changes in wet season duration

318   implied by these changes in onset and demise dates, the future scenario indicates an increase in

319   wet season precipitation over most of the northern hemisphere monsoon zones, and a decrease

320   over much of South America and southern Africa (Fig. 7C). These projections, which broadly

321   correspond to an increase in wet season rainfall in the northern hemisphere and a decrease in the

14

322   southern hemisphere, are consistent with projections from previous CMIP phases (Bombardi and

323   Carvalho 2009; Seth et al. 2010; Fan et al. 2012; Qing 2012; Jiang and Tian 2013; Jourdain et al.

324   2013; Menon et al. 2013; Li et al. 2015; Sooraj et al. 2015; Monerie et al. 2012; Biasutti 2013;

325   Roehrig et al. 2013), and more recent studies focusing on CMIP6 (e.g. Ha et al. 2020; Wang et

326   al. 2020). Over northern Australia, there is little agreement among models regarding a change in

327   wet season precipitation or a change in the timing of the wet season (Fig. 7), consistent with the

328   findings of Narsey et al. (2020).

329

330   **5. Possible energetic controls on rainfall trends**

331   **a.   Motivating and defining the relative MSE**

332   In this section we analyze surface air (2 meter) MSE and its changes to better understand

333   the mechanisms whereby climate change might affect monsoon rainfall. Most monsoon regions

334   are sites of local maxima in surface air MSE (Fig. 8), with idealized theory predicting that

335   monsoon rainfall should be concentrated on the equatorial side of these maxima (Nie et al.

336   2010). Surface air MSE is not a boundary condition or forcing for monsoons, but is set

337   interactively by surface enthalpy fluxes, radiative cooling, and horizontal advection;

338   nevertheless, its relationship with moist convective activity often allows the three-dimensional

339   circulation and the precipitation field to be understood in terms of the two-dimensional MSE

340   field (see review by Neelin 2007).

341   As discussed in the Introduction, it has been argued that monsoon onset will be delayed

342   in a warming world if near-surface MSE in monsoon regions during early summer does not

343   increase as rapidly as is needed to maintain convective instability given the free-tropospheric

344   warming (Seth et al. 2011). In an attempt to quantify this effect, Seth et al. (2013) evaluated

15

345   changes in atmospheric convective stability between historical and future scenario runs using the

346   discretized vertical gradient of MSE (200hPa MSE minus 850hPa MSE). However, that vertical

347   MSE gradient does not quantify known measures of convective stability. In particular, an

348   atmospheric column is potentially unstable if its equivalent potential temperature (which is

349   closely related to MSE) decreases upward, but this is a binary measure with a column being

350   potentially stable or unstable; a quantitative measure is the convective available potential energy

351   (CAPE), which can be approximated by differences of near-surface MSE and the *saturation*

352   value of free-tropospheric MSE (e.g. Emanuel et al. 1994).

353   Thus, rather than use the Seth et al. (2013) metric, we note that the CQE frameworks on

354   which the upped-ante idea is based (Chou and Neelin 2004) assume that tropospheric

355   temperature in much of the tropics is set by near-surface MSE in convecting regions.

356   Specifically, if near-surface MSE in a convecting region increases by Δh, gravity waves will

357   spread any free-tropospheric warming throughout the tropics and thus require that all remote

358   regions undergo an increase of Δh in their near-surface MSE in order to maintain a constant

359   degree of convective instability. Such relationships have been shown to couple near-surface

360   MSE over land and ocean in observations (Zhang and Fueglistaler 2020). This motivates us to

361   define the "relative MSE" as the local near-surface MSE minus the tropical mean (20°S-20°N;

362   all longitudes, land and ocean) near-surface MSE. This is a generalization of "relative sea surface

363   temperature (SST)", which has been influential in understanding variations in tropical cyclone

364   activity (Vecchi and Soden 2007; Swanson 2008; Ramsay and Sobel 2011), with an important

365   aspect of this generalization being that it is defined in land regions (unlike relative SST). A

366   possible benefit of both relative MSE and relative SST is that they capture the local and large-

367   scale forcings for convection, rather than relying on local, column-wise measures such as CAPE

16

368 or the local vertical gradient of MSE (Seth et al. 2013) that are expected to be rapidly adjusted by

369 convective activity.

370   In every monsoon region, surface air MSE reaches its peak in summer, between the local

371 onset and demise dates (Fig. 9). In each region, the MSE has roughly the same value on the

372 onset date as on the demise date; since these dates are defined using only precipitation, this lends

373 confidence in the connection of MSE to precipitation and the timing of the rainy season.

374 Additionally, some of the most prominent CMIP6 biases in monsoons are consistent with the

375 MSE biases: large negative MSE biases over India and South America from winter through

376 early summer accompany the late onset biases in those regions (Fig. 9C,D). There is variability

377 across regions in the MSE values at which onset and demise occur, ranging from about 340 kJ

378 kg^{-1} in North America and the Sahel to 350 kJ kg^{-1} in India; since the tropical mean surface air

379 MSE is around 339 kJ kg^{-1}, with relatively little seasonal and interannual variation (not shown),

380 onset and demise occur at different relative MSE values in each region. This is not surprising,

381 given the many assumptions and simplifications involved in relating large-scale precipitating

382 circulations to surface air MSE. So we hypothesize that the rainy season begins when the

383 relative MSE first increases beyond some threshold, with this threshold varying between regions

384 due to differences in factors that might affect the relation of relative MSE to precipitation, such

385 as free-tropospheric dry air intrusions (Parker et al. 2016) and the vertical structure of ascent

386 (Back and Bretherton 2006). We furthermore hypothesize that this relative MSE threshold will

387 remain invariant under climate change within each region; this is examined further below.

388

389   **b. Future changes in relative MSE**

390   As expected in a warming world, the models indicate an increase in mean near-surface

391   MSE for all days of the year under scenarios SSP3.70 and SSP5.85, compared to historical runs.

392   The mean annual cycle of relative MSE in monsoon regions has similar temporal structure for

393   historical and future scenario simulations, reaching minimum values during local winter and

394   maximum values during summer (Fig. 9). Figure 10 shows the mean annual cycle of the change

395   in relative MSE between scenario (SSP5.85) and historical runs; positive values occur when a

396   region's near-surface MSE increases more than that of the rest of the tropics, indicating an

397   expected future increase in convective instability. Over all core monsoonal regions, relative MSE

398   differences are generally positive during the wet season and negative during the dry season. This

399   is consistent with findings of Giannini (2010) and Seth et al. (2013), who argued that models

400   show a dominance of free-tropospheric warming and thus greater convective stability in winter,

401   while near-surface warming and moistening and thus greater instability dominated in summer.

402   Of course, true convective stability involves the full vertical structure of temperature and

403   humidity, especially when one accounts for possible entrainment of environmental air into

404   clouds (e.g. Emanuel et al. 1994; Derbyshire et al. 2004), so these changes in relative MSE are

405   crude and incomplete indicators of the combined local and remote forcings for convective

406   activity; we do not claim that a mean summer increase in relative MSE signifies a larger mean

407   summer convective mass flux.

408   The more salient features seen in Fig. 10 are the future changes in relative MSE occurring

409   around onset and demise dates. Most prominent are the increases in relative MSE before

410   monsoon onset and after demise in India (Fig. 10,C), which are accompanied by the earlier onset

411   and later demise expected in our relative MSE framework. The Sahel also shows a large increase

412   in relative MSE in late summer, together with a future delay in its demise date (Fig. 10B). Both

18

413   South America and southern Africa show reductions in relative MSE near the historical onset

414   date, and the corresponding expected delay in future onset (Fig. 10D, E).

415   Other changes in relative MSE near onset and demise dates are smaller, at least in the

416   multi-model mean shown in Fig. 10, which motivates inspection of the intermodel variations in

417   changes in both relative MSE and onset/demise dates. There is a strong correlation between

418   future changes in relative MSE in a region and future changes in its onset/demise dates (Fig. 11).

419   As expected by the logic used to motivate our construction of the relative MSE diagnostic,

420   models with larger future increases in relative MSE in early summer exhibit earlier onset, and

421   models with larger future increases in relative MSE in late summer exhibit later demise. The

422   intermodel variability in the relative MSE changes explains 50-80% of the intermodel variance

423   in onset and demise dates, and the coefficients of the best linear fit to intermodel variability for

424   the SSP3.70 scenario are nearly the same as those for the SSP5.85 scenario. The linear fits

425   indicate that, for no change in relative MSE, there is a delay in onset and an earlier demise by

426   roughly five days; in other words, to maintain the same onset date an increase in relative MSE is

427   required. We do not investigate here whether this results from error in the fit, an expected

428   relationship between relative MSE and convective onset in a warming world, a peculiarity of

429   model convection schemes, a result of changes in tropical-mean near-surface MSE in regions

430   that are convectively stable, or some other factor.

431

432   c. **Meridional gradients in MSE**

433   Although changes in relative MSE are strongly correlated with changes in onset and

434   demise dates (Fig. 11), the former cannot be viewed as causing the latter because MSE can be

435   rapidly altered by horizontal advection, radiation, and surface fluxes. Some constraint on the

19

436   large-scale processes that influence monsoon-region MSE or tropical-mean MSE would be better

437   viewed as a cause, and here we draw attention to changes in the tropical-extratropical contrast in

438   MSE in the model projections. This contrast is central to vertically integrated energy budget

439   frameworks that link changes in monsoon precipitation to changes in meridional energy fluxes

440   (Kang et al. 2008; Schneider et al. 2014; Boos and Korty 2016), which in turn scale with the

441   magnitude of the meridional gradient in surface air MSE under a diffusive approximation

442   (Hwang and Frierson 2010; Merlis and Henry 2018; Peterson and Boos 2020).

443   Figure 12 presents spatial distributions of relative MSE changes during the onset and

444   demise periods for four core monsoon regions. Relative MSE changes are averaged over all

445   models and over the month when each model's median onset (or demise) date occurs in

446   historical runs, with this procedure performed for each core monsoon region. The spatial patterns

447   of relative MSE changes are similar for monsoons from the same hemisphere (not shown), so

448   results for India are showed in Figure 12A,C and results for South America in Figure 12B,D. The

449   figure also includes zonal means of the relative MSE change for those two regions (solid lines in

450   left panels) as well as zonal means for the months of onset and demise over the Sahel and

451   southern Africa (dashed lines in left panels).

452   The most prominent pattern is the large meridional gradient in the change of relative

453   MSE, which has greatest magnitude in the southern hemisphere. That is, in the southern

454   hemisphere of a warming world, monsoon regions undergo onset and demise in a hemispheric

455   background state possessing an enhanced tropical-extratropical MSE gradient. One would expect

456   this enhanced meridional MSE gradient to facilitate greater advection of low-MSE air into the

457   southern hemisphere monsoon regions, or equivalently a vertically integrated flux of MSE out of

458   those regions (e.g. Hwang and Frierson 2010), decreasing the local monsoon-region MSE and

20

459 reducing rainfall. Indeed, rainy season onset is delayed in projections of most of the southern

460 hemisphere regions (Fig. 12B), demise occurs earlier (Fig. 12D), and wet season precipitation is

461 reduced (Fig. 7C). Northern Australia is a partial exception to this pattern, with less agreement

462 between models there. The Northern Hemisphere monsoon regions undergo onset in a global

463 background state with relatively little change in that hemisphere's tropical-extratropical MSE

464 gradient (Fig. 12A), and the northern hemisphere exhibits a general dominance of earlier onset

465 (Fig. 12A), later demise (Fig. 12C), and more wet season precipitation (not shown, but similar to

466 Fig. 7C). We speculate that a general increase in amplitude of the seasonal cycle of rainfall

467 would occur in a warming world with no change in meridional MSE gradient due to greater

468 moisture content (e.g. Held and Soden 2006), leading to earlier onset, later demise, and more wet

469 season rainfall; this overall enhancement of rainfall would then be the background change that is

470 opposed in the southern hemisphere by the enhanced tropical-extratropical MSE gradient.

471

472 **6. Conclusions**

473   We evaluated the representation of the characteristics of the wet season over core

474 monsoonal regions by a subset of simulations performed as part of the new WCRP-CMIP6. We

475 also investigated future projections of the characteristics of the wet season in a subset of CMIP6

476 models. Our analysis included evaluation of the seasonal cycle of precipitation, the timing of the

477 wet season, and the accumulated precipitation during the wet season. We also investigated the

478 role of atmospheric stability, as measured by relative MSE, in changing the precipitation

479 seasonal cycle.

480   The characteristics of the wet season (onset, demise, and accumulated precipitation) were

481 calculated using a consistent method across monsoonal regions based on the RADS methodology

21

482   by Bombardi et al. (2019). We find that, in general, the summer monsoon in the central Sahel

483   and Asia is projected to withdraw later and become wetter in comparison to historical runs. In

484   contrast, the summer monsoon over South America and southern Africa are projected to start

485   later and become drier in comparison to historical runs.

486   The models still have serious deficiencies in representing tropical precipitation. Among

487   some of the most concerning problems are:

488   • poor representations of the seasonal cycle of precipitation over the North American

489   monsoon domain, especially during the withdrawal of the wet season.

490   • poor representation of the onset of the Indian monsoon and an overall dry bias over the

491   Indian and East Asian monsoon domains;

492   • dry bias over the Amazon region and wet bias over northeast Brazil; and to a lesser

493   extent, dry biases over the Sahel.

494   Although accurate simulation of present-day climate does not guarantee reliable

495   projection of the future, it seems worthwhile to clearly state the projections for regions that do

496   have low bias in their historical simulations. These include:

497   • A very likely shortening of the wet season over South America (later onset and early

498   demises), associated with a decrease in total rainfall during the rainy season.

499   • A likely shortening of the wet season over southern Africa (late onsets) associated with a

500   decrease in mean total rainfall during the rainy season over southern Africa.

501   • An extension of the wet season over India (later demises) associated with an increase in

502   wet season rainfall, which is consistent with previous studies (e.g. Wang et al. 2020a,b).

503   However, uncertainties in the representation of the onset date of the Indian monsoon

22

504   suggest that these projections should be interpreted with caution since the model

505   simulations of early summer rainfall are strongly biased.

506   • There is substantial spatial variability in the characteristics of the rainy season over West

507   Africa and the Sahel. Therefore, changes in wet season characteristics across the Sahel

508   due to climate change may vary from region to region. For example, projections show

509   different results for coastal West Africa and the continental Sahel. Over the core region

510   we selected to study, the models project an extension of the wet season (later demises)

511   associated with an increase in wet season precipitation. However, uncertainties in

512   observations and simulations suggest that these projections should be interpreted with

513   caution.

514   • There is no agreement in models' projections for the timing of the wet season or in the

515   accumulated precipitation during the wet season over northern Australia, consistent with

516   Narsey et al. (2020).

517   Future projections of changes in the timing of monsoons are well captured by changes in

518 near-surface relative MSE. Simulations indicate that the Sahel and India will experience longer

519 wet seasons associated with near-surface MSE increasing in those regions by more than the

520 tropical mean during the historical onset and demise periods. The opposite is expected for South

521 America and southern Africa, which have decreases in relative MSE during the historical onset

522 periods. In the southern hemisphere, where those two regions lie, the tropical-extratropical

523 gradient in MSE is projected to increase, which we speculate might lead to more cold and dry

524 extratropical air penetrating into those regions (or, equivalently, more quasi-diffusive transport

525 of MSE out of those regions). Although meridional fluxes of MSE between monsoon regions

526 and higher latitudes have been shown to cause rainfall changes in monsoon regions (e.g., Kang et

23

527　al. 2008; Boos and Korty 2016; Peterson and Boos 2020), further work is needed to determine

528　whether the Southern Hemisphere's enhanced meridional MSE gradient in future projections

529　truly causes the shortening of that hemisphere's summer monsoons.

530　　　The dry biases over India, eastern Asia, and the Amazon are deficiencies that have been

531　present in climate models since CMIP3. In addition, the models still show large deficiencies in

532　representing precipitation in convergence zones (such as MBF, SPCZ, and SACZ) associated

533　with monsoon systems. Without a better representation of these features, confidence in future

534　projections of climate change over regions affected by these features (i.e. southeastern Brazil and

535　eastern China) is compromised.

536　　　Although many of the analyses presented in this study show results for all regions within

537　45 degrees of the equator, these analyses are most reliable over monsoonal regions. While some

538　regions in midlatitudes, such as the Great Plains in the United States, experience moderate

539　precipitation seasonality, the definition of onset and demise dates over these regions is less

540　accurate than over monsoonal regions (Bombardi et al. 2019). Therefore, projections of future

541　changes in onset and demise dates and wet season precipitation over these regions should be

542　interpreted with caution.

543

24

559

560 **References**
561 Abram, N., and Coauthors, 2019: *Framing and Context of the Report Supplementary Material.*
562   *In: IPCC Special Report on the Ocean and Cryosphere in a Changing Climate*. 11 pp.
563 Adler, R. F., and Coauthors, 2003: The Version-2 Global Precipitation Climatology Project
564   (GPCP) Monthly Precipitation Analysis (1979–Present). *J. Hydrometeorol.*, **4**, 1147–1167,
565   https://doi.org/10.1175/1525-7541(2003)004<1147:TVGPCP>2.0.CO;2.
566 Arakawa, A., and W. H. Schubert, 1974: Interaction of a Cumulus Cloud Ensemble with the
567   Large-Scale Environment, Part I. *J. Atmos. Sci.*, **31**, 674–701, https://doi.org/10.1175/1520-
568   0469(1974)031<0674:IOACCE>2.0.CO;2.
569 Back, L. E., and C. S. Bretherton, 2006: Geographic variability in the export of moist static
570   energy and vertical motion profiles in the tropical Pacific. *Geophys. Res. Lett.*, **33**, L17810,
571   https://doi.org/10.1029/2006GL026672.
572 Biasutti, M., 2013: Forced Sahel rainfall trends in the CMIP5 archive. *J. Geophys. Res. Atmos.*,
573   **118**, 1613–1623, https://doi.org/10.1002/jgrd.50206.
574 Biasutti, M., and A. H. Sobel, 2009: Delayed Sahel rainfall and global seasonal cycle in a
575   warmer climate. *Geophys. Res. Lett.*, **36**, L23707, https://doi.org/10.1029/2009GL041303.
576 Bombardi, R. J., and L. M. V. Carvalho, 2008: Variability of the monsoon regime over the
577   Brazilian Savanna: the present climate and projections for a 2xCO2 scenario using the
578   MIROC model. *Rev. Bras. Meteorol.*, **23**, 58–72, https://doi.org/10.1590/S0102-
579   77862008000100007.
580 Bombardi, R. J., and L. M. V. Carvalho, 2009: IPCC global coupled model simulations of the
581   South America monsoon system. *Clim. Dyn.*, **33**, 893–916, https://doi.org/10.1007/s00382-
582   008-0488-1.
583 ——, J. L. Kinter, and O. W. Frauenfeld, 2019: A Global Gridded Dataset of the Characteristics
584   of the Rainy And Dry Seasons. *Bull. Am. Meteorol. Soc.*, **100**, 1315–1328,
585   https://doi.org/10.1175/BAMS-D-18-0177.1.

586 Boos, W. R., and R. L. Korty, 2016: Regional energy budget control of the intertropical
587   convergence zone and application to mid-Holocene rainfall. *Nat. Geosci.*, **9**, 892–897,
588   https://doi.org/10.1038/ngeo2833.

589 Boucher, O., S. Denvil, A. Caubel, and M. A. Foujols, 2018: IPSL IPSL-CM6A-LR model
590   output prepared for CMIP6 CMIP. https://doi.org/10.22033/ESGF/CMIP6.1534.

591 Brown, J. N., and Coauthors, 2013: Implications of CMIP3 model biases and uncertainties for
592   climate projections in the western tropical Pacific. *Clim. Change*, **119**, 147–161,
593   https://doi.org/10.1007/s10584-012-0603-5.

594 Cao, J., and B. Wang, 2019: NUIST NESMv3 model output prepared for CMIP6 CMIP.
595   https://doi.org/10.22033/ESGF/CMIP6.2021.

596 Chen, Z., T. Zhou, L. Zhang, X. Chen, W. Zhang, and J. Jiang, 2020: Global Land Monsoon
597   Precipitation Changes in CMIP6 Projections. *Geophys. Res. Lett.*, **47**,
598   https://doi.org/10.1029/2019GL086902.

599 Chou, C., and J. D. Neelin, 2001: Mechanisms limiting the southward extent of the South
600   American Summer Monsoon. *Geophys. Res. Lett.*, **28**, 2433–2436,
601   https://doi.org/10.1029/2000GL012138.

602 ——, and ——, 2003: Mechanisms Limiting the Northward Extent of the Northern Summer
603   Monsoons over North America, Asia, and Africa*. *J. Clim.*, **16**, 406–425,
604   https://doi.org/10.1175/1520-0442(2003)016<0406:MLTNEO>2.0.CO;2.

605 ——, and ——, 2004: Mechanisms of Global Warming Impacts on Regional Tropical
606   Precipitation*. *J. Clim.*, **17**, 2688–2701, https://doi.org/10.1175/1520-
607   0442(2004)017<2688:MOGWIO>2.0.CO;2.

608 Chou, C., J. D. Neelin, and H. Su, 2001: Ocean-atmosphere-land feedbacks in an idealized
609   monsoon. *Q. J. R. Meteorol. Soc.*, **127**, 1869–1891,
610   https://doi.org/10.1002/qj.49712757602.

611 Cook, B. I., and R. Seager, 2013: The response of the North American Monsoon to increased
612   greenhouse gas forcing. *J. Geophys. Res. Atmos.*, **118**, 1690–1699,
613   https://doi.org/10.1002/jgrd.50111.

614 Creese, A., and R. Washington, 2018: A Process-Based Assessment of CMIP5 Rainfall in the
615   Congo Basin: The September–November Rainy Season. *J. Clim.*, **31**, 7417–7439,
616   https://doi.org/10.1175/JCLI-D-17-0818.1.

617 Danabasoglu, G., 2019a: NCAR CESM2 model output prepared for CMIP6 CMIP historical.
618   https://doi.org/10.22033/ESGF/CMIP6.7627.

619 ——, 2019b: NCAR CESM2-WACCM model output prepared for CMIP6 CMIP.
620   https://doi.org/10.22033/ESGF/CMIP6.10024.

621 Derbyshire, S. H., I. Beau, P. Bechtold, J.-Y. Grandpeix, J.-M. Piriou, J.-L. Redelsperger, and P.
622   M. M. Soares, 2004: Sensitivity of moist convection to environmental humidity. *Q. J. R.
623   Meteorol. Soc.*, **130**, 3055–3079, https://doi.org/10.1256/qj.03.130.

624 Emanuel, K. A., J. David Neelin, and C. S. Bretherton, 1994: On large-scale circulations in
625   convecting atmospheres. *Q. J. R. Meteorol. Soc.*, **120**, 1111–1143,
626   https://doi.org/10.1002/qj.49712051902.

627 Fan, F., M. E. Mann, S. Lee, and J. L. Evans, 2012: Future Changes in the South Asian Summer
628   Monsoon: An Analysis of the CMIP3 Multimodel Projections. *J. Clim.*, **25**, 3909–3928,
629   https://doi.org/10.1175/JCLI-D-11-00133.1.

630 Fiedler, S., and Coauthors, 2020: Simulated Tropical Precipitation Assessed across Three Major
631   Phases of the Coupled Model Intercomparison Project (CMIP). *Mon. Weather Rev.*, **148**,

632   3653–3680, https://doi.org/10.1175/MWR-D-19-0404.1.

633   Funk, C., and Coauthors, 2015: The climate hazards infrared precipitation with stations—a new
634   environmental record for monitoring extremes. *Sci. Data*, **2**, 150066,
635   https://doi.org/10.1038/sdata.2015.66.

636   Gaetani, M., C. Flamant, S. Bastin, S. Janicot, C. Lavaysse, F. Hourdin, P. Braconnot, and S.
637   Bony, 2017: West African monsoon dynamics and precipitation: the competition between
638   global SST warming and CO2 increase in CMIP5 idealized simulations. *Clim. Dyn.*, **48**,
639   1353–1373, https://doi.org/10.1007/s00382-016-3146-z.

640   Geil, K. L., Y. L. Serra, and X. Zeng, 2013: Assessment of CMIP5 Model Simulations of the
641   North American Monsoon System. *J. Clim.*, **26**, 8787–8801, https://doi.org/10.1175/JCLI-
642   D-13-00044.1.

643   Giannini, A., 2010: Mechanisms of Climate Change in the Semiarid African Sahel: The Local
644   View. *J. Clim.*, **23**, 743–756, https://doi.org/10.1175/2009JCLI3123.1.

645   Grose, M. R., and Coauthors, 2014: Assessment of the CMIP5 global climate model simulations
646   of the western tropical Pacific climate system and comparison to CMIP3. *Int. J. Climatol.*,
647   **34**, 3382–3399, https://doi.org/10.1002/joc.3916.

648   Gulizia, C., and I. Camilloni, 2015: Comparative analysis of the ability of a set of CMIP3 and
649   CMIP5 global climate models to represent precipitation in South America. *Int. J. Climatol.*,
650   **35**, 583–595, https://doi.org/10.1002/joc.4005.

651   Guo, H., and Coauthors, 2018: NOAA-GFDL GFDL-CM4 model output.
652   https://doi.org/10.22033/ESGF/CMIP6.1402.

653   Gusain, A., S. Ghosh, and S. Karmakar, 2020: Added value of CMIP6 over CMIP5 models in
654   simulating Indian summer monsoon rainfall. *Atmos. Res.*, **232**, 104680,
655   https://doi.org/10.1016/j.atmosres.2019.104680.

656   Ha, K., S. Moon, A. Timmermann, and D. Kim, 2020: Future Changes of Summer Monsoon
657   Characteristics and Evaporative Demand Over Asia in CMIP6 Simulations. *Geophys. Res.*
658   *Lett.*, **47**, https://doi.org/10.1029/2020GL087492.

659   He, C., T. Li, and W. Zhou, 2020: Drier North American Monsoon in Contrast to Asian–African
660   Monsoon under Global Warming. *J. Clim.*, **33**, 9801–9816, https://doi.org/10.1175/JCLI-D-
661   20-0189.1.

662   Held, I. M., and B. J. Soden, 2006: Robust Responses of the Hydrological Cycle to Global
663   Warming. *J. Clim.*, **19**, 5686–5699, https://doi.org/10.1175/JCLI3990.1.

664   Hersbach, H., and Coauthors, 2020: The ERA5 global reanalysis. *Q. J. R. Meteorol. Soc.*, **146**,
665   1999–2049, https://doi.org/10.1002/qj.3803.

666   Hsu, P., T. Li, H. Murakami, and A. Kitoh, 2013: Future change of the global monsoon revealed
667   from 19 CMIP5 models. *J. Geophys. Res. Atmos.*, **118**, 1247–1260,
668   https://doi.org/10.1002/jgrd.50145.

669   Huffman, G. J., and Coauthors, 2007: The TRMM Multisatellite Precipitation Analysis (TMPA):
670   Quasi-Global, Multiyear, Combined-Sensor Precipitation Estimates at Fine Scales. *J.*
671   *Hydrometeorol.*, **8**, 38–55, https://doi.org/10.1175/JHM560.1.

672   Huo-Po, C., and S. Jian-Qi, 2013: How Large Precipitation Changes over Global Monsoon
673   Regions by CMIP5 Models? *Atmos. Ocean. Sci. Lett.*, **6**, 306–311.

674   Hwang, Y.-T., and D. M. W. Frierson, 2010: Increasing atmospheric poleward energy transport
675   with global warming. *Geophys. Res. Lett.*, **37**, n/a-n/a,
676   https://doi.org/10.1029/2010GL045440.

677   Jiang, D., and Z. Tian, 2013: East Asian monsoon change for the 21st century: Results of CMIP3

and CMIP5 models. *Chinese Sci. Bull.*, **58**, 1427–1435, https://doi.org/10.1007/s11434-012-5533-0.

Jin, C., B. Wang, and J. Liu, 2020: Future Changes and Controlling Factors of the Eight Regional Monsoons Projected by CMIP6 Models. *J. Clim.*, **33**, 9307–9326, https://doi.org/10.1175/JCLI-D-20-0236.1.

Joetzjer, E., H. Douville, C. Delire, and P. Ciais, 2013: Present-day and future Amazonian precipitation in global climate models: CMIP5 versus CMIP3. *Clim. Dyn.*, **41**, 2921–2936, https://doi.org/10.1007/s00382-012-1644-1.

Jones, C., and L. M. V. Carvalho, 2013: Climate Change in the South American Monsoon System: Present Climate and CMIP5 Projections. *J. Clim.*, **26**, 6660–6678, https://doi.org/10.1175/JCLI-D-12-00412.1.

Jourdain, N. C., A. Sen Gupta, A. S. Taschetto, C. C. Ummenhofer, A. F. Moise, and K. Ashok, 2013: The Indo-Australian monsoon and its relationship to ENSO and IOD in reanalysis data and the CMIP3/CMIP5 simulations. *Clim. Dyn.*, **41**, 3073–3102, https://doi.org/10.1007/s00382-013-1676-1.

Kang, S. M., I. M. Held, D. M. W. Frierson, and M. Zhao, 2008: The Response of the ITCZ to Extratropical Thermal Forcing: Idealized Slab-Ocean Experiments with a GCM. *J. Clim.*, **21**, 3521–3532, https://doi.org/10.1175/2007JCLI2146.1.

Kim, H.-J., B. Wang, and Q. Ding, 2008: The Global Monsoon Variability Simulated by CMIP3 Coupled Climate Models*. *J. Clim.*, **21**, 5271–5294, https://doi.org/10.1175/2008JCLI2041.1.

Krasting, J. P., and Coauthors, 2018: NOAA-GFDL GFDL-ESM4 model output prepared for CMIP6 CMIP historical. https://doi.org/10.22033/ESGF/CMIP6.8597.

Kriegler, E., and Coauthors, 2017: Fossil-fueled development (SSP5): An energy and resource intensive scenario for the 21st century. *Glob. Environ. Chang.*, **42**, 297–315, https://doi.org/10.1016/j.gloenvcha.2016.05.015.

Kusunoki, S., and O. Arakawa, 2015: Are CMIP5 Models Better than CMIP3 Models in Simulating Precipitation over East Asia? *J. Clim.*, **28**, 5601–5621, https://doi.org/10.1175/JCLI-D-14-00585.1.

Lambert, S. J., and G. J. Boer, 2001: CMIP1 evaluation and intercomparison of coupled climate models. *Clim. Dyn.*, **17**, 83–106, https://doi.org/10.1007/PL00013736.

Lee, J.-Y., and B. Wang, 2014: Future change of global monsoon in the CMIP5. *Clim. Dyn.*, **42**, 101–119, https://doi.org/10.1007/s00382-012-1564-0.

Li, G., and S.-P. Xie, 2014: Tropical Biases in CMIP5 Multimodel Ensemble: The Excessive Equatorial Pacific Cold Tongue and Double ITCZ Problems*. *J. Clim.*, **27**, 1765–1780, https://doi.org/10.1175/JCLI-D-13-00337.1.

Li, X., M. Ting, C. Li, and N. Henderson, 2015: Mechanisms of Asian Summer Monsoon Changes in Response to Anthropogenic Forcing in CMIP5 Models*. *J. Clim.*, **28**, 4107–4125, https://doi.org/10.1175/JCLI-D-14-00559.1.

Liebmann, B., and J. A. Marengo, 2001: Interannual Variability of the Rainy Season and Rainfall in the Brazilian Amazon Basin. *J. Clim.*, **14**, 4308–4318, https://doi.org/10.1175/1520-0442(2001)014<4308:IVOTRS>2.0.CO;2.

Maloney, E. D., and Coauthors, 2014: North American Climate in CMIP5 Experiments: Part III: Assessment of Twenty-First-Century Projections*. *J. Clim.*, **27**, 2230–2270, https://doi.org/10.1175/JCLI-D-13-00273.1.

Menon, A., A. Levermann, J. Schewe, J. Lehmann, and K. Frieler, 2013: Consistent increase in

Indian monsoon rainfall and its variability across CMIP-5 models. *Earth Syst. Dyn.*, **4**, 287–300, https://doi.org/10.5194/esd-4-287-2013.

Merlis, T. M., and M. Henry, 2018: Simple Estimates of Polar Amplification in Moist Diffusive Energy Balance Models. *J. Clim.*, **31**, 5811–5824, https://doi.org/10.1175/JCLI-D-17-0578.1.

Monerie, P.-A., B. Fontaine, and P. Roucou, 2012: Expected future changes in the African monsoon between 2030 and 2070 using some CMIP3 and CMIP5 models under a medium-low RCP scenario. *J. Geophys. Res. Atmos.*, **117**, n/a-n/a, https://doi.org/10.1029/2012JD017510.

Moon, S., and K.-J. Ha, 2020: Future changes in monsoon duration and precipitation using CMIP6. *npj Clim. Atmos. Sci.*, **3**, 45, https://doi.org/10.1038/s41612-020-00151-w.

Narsey, S. Y., J. R. Brown, R. A. Colman, F. Delage, S. B. Power, A. F. Moise, and H. Zhang, 2020: Climate Change Projections for the Australian Monsoon From CMIP6 Models. *Geophys. Res. Lett.*, **47**, https://doi.org/10.1029/2019GL086816.

Neelin, J. D., 2007: Moist dynamics of tropical convection zones in monsoons, teleconnections and global warming. *The Global Circulation of the Atmosphere*, T. Schneider and A. Sobel, Eds., Princeton University Press, Princeton and Oxford, p. 385.

Neelin, J. D., and I. M. Held, 1987: Modeling Tropical Convergence Based on the Moist Static Energy Budget. *Mon. Weather Rev.*, **115**, 3–12, https://doi.org/10.1175/1520-0493(1987)115<0003:MTCBOT>2.0.CO;2.

Nie, J., W. R. Boos, and Z. Kuang, 2010: Observational Evaluation of a Convective Quasi-Equilibrium View of Monsoons. *J. Clim.*, **23**, 4416–4428, https://doi.org/10.1175/2010JCLI3505.1.

Niznik, M. J., B. R. Lintner, A. J. Matthews, and M. J. Widlansky, 2015: The Role of Tropical–Extratropical Interaction and Synoptic Variability in Maintaining the South Pacific Convergence Zone in CMIP5 Models. *J. Clim.*, **28**, 3353–3374, https://doi.org/10.1175/JCLI-D-14-00527.1.

Oueslati, B., and G. Bellon, 2015: The double ITCZ bias in CMIP5 models: interaction between SST, large-scale circulation and precipitation. *Clim. Dyn.*, **44**, 585–607, https://doi.org/10.1007/s00382-015-2468-6.

Parker, D. J., P. Willetts, C. Birch, A. G. Turner, J. H. Marsham, C. M. Taylor, S. Kolusu, and G. M. Martin, 2016: The interaction of moist convection and mid-level dry air in the advance of the onset of the Indian monsoon. *Q. J. R. Meteorol. Soc.*, **142**, 2256–2272, https://doi.org/10.1002/qj.2815.

Peterson, H. G., and W. R. Boos, 2020: Feedbacks and eddy diffusivity in an energy balance model of tropical rainfall shifts. *npj Clim. Atmos. Sci.*, **3**, 11, https://doi.org/10.1038/s41612-020-0114-4.

Qing, B., 2012: Projected Changes in Asian Summer Monsoon in RCP Scenarios of CMIP5. *Atmos. Ocean. Sci. Lett.*, **5**, 43–48, https://doi.org/10.1080/16742834.2012.11446959.

Ramsay, H. A., and A. H. Sobel, 2011: Effects of Relative and Absolute Sea Surface Temperature on Tropical Cyclone Potential Intensity Using a Single-Column Model. *J. Clim.*, **24**, 183–193, https://doi.org/10.1175/2010JCLI3690.1.

Riahi, K., and Coauthors, 2017: The Shared Socioeconomic Pathways and their energy, land use, and greenhouse gas emissions implications: An overview. *Glob. Environ. Chang.*, **42**, 153–168, https://doi.org/10.1016/j.gloenvcha.2016.05.009.

Rienecker, M. M., and Coauthors, 2012: *Atmospheric Reanalyses—Recent Progress and*

770   *Prospects for the Future. NASA Tech. Rep. Series on Global Modeling and Data*
771   *Assimilation, NASA/TM–2012-104606/Vol 29*. 48pp pp.
772   http://gmao.gsfc.nasa.gov/pubs/docs/NASATM2012-104606v29.pdf.
773 Roehrig, R., D. Bouniol, F. Guichard, F. Hourdin, and J.-L. Redelsperger, 2013: The Present and
774   Future of the West African Monsoon: A Process-Oriented Assessment of CMIP5
775   Simulations along the AMMA Transect. *J. Clim.*, **26**, 6471–6505,
776   https://doi.org/10.1175/JCLI-D-12-00505.1.
777 Schneider, T., T. Bischoff, and G. H. Haug, 2014: Migrations and dynamics of the intertropical
778   convergence zone. *Nature*, **513**, 45–53, https://doi.org/10.1038/nature13636.
779 Seferian, R., 2018: CNRM-CERFACS CNRM-ESM2-1 model output prepared for CMIP6
780   CMIP historical. https://doi.org/10.22033/ESGF/CMIP6.4068.
781 Séférian, R., and Coauthors, 2016: Development and evaluation of CNRM Earth system model –
782   CNRM-ESM1. *Geosci. Model Dev.*, **9**, 1423–1453, https://doi.org/10.5194/gmd-9-1423-
783   2016.
784 Seo, K.-H., J. Ok, J.-H. Son, and D.-H. Cha, 2013: Assessing Future Changes in the East Asian
785   Summer Monsoon Using CMIP5 Coupled Models. *J. Clim.*, **26**, 7662–7675,
786   https://doi.org/10.1175/JCLI-D-12-00694.1.
787 Seth, A., M. Rojas, and S. A. Rauscher, 2010: CMIP3 projected changes in the annual cycle of
788   the South American Monsoon. *Clim. Change*, **98**, 331–357, https://doi.org/10.1007/s10584-
789   009-9736-6.
790 ——, S. A. Rauscher, M. Rojas, A. Giannini, and S. J. Camargo, 2011: Enhanced spring
791   convective barrier for monsoons in a warmer world? *Clim. Change*, **104**, 403–414,
792   https://doi.org/10.1007/s10584-010-9973-8.
793 ——, ——, M. Biasutti, A. Giannini, S. J. Camargo, and M. Rojas, 2013: CMIP5 Projected
794   Changes in the Annual Cycle of Precipitation in Monsoon Regions. *J. Clim.*, **26**, 7328–
795   7351, https://doi.org/10.1175/JCLI-D-12-00726.1.
796 Sharmila, S., S. Joseph, A. K. Sahai, S. Abhilash, and R. Chattopadhyay, 2015: Future projection
797   of Indian summer monsoon variability under climate change scenario: An assessment from
798   CMIP5 climate models. *Glob. Planet. Change*, **124**, 62–78,
799   https://doi.org/10.1016/j.gloplacha.2014.11.004.
800 Sheffield, J., and Coauthors, 2013: North American Climate in CMIP5 Experiments. Part I:
801   Evaluation of Historical Simulations of Continental and Regional Climatology. *J. Clim.*, **26**,
802   9209–9245, https://doi.org/10.1175/JCLI-D-12-00592.1.
803 Song, F., and T. Zhou, 2014: Interannual Variability of East Asian Summer Monsoon Simulated
804   by CMIP3 and CMIP5 AGCMs: Skill Dependence on Indian Ocean–Western Pacific
805   Anticyclone Teleconnection. *J. Clim.*, **27**, 1679–1697, https://doi.org/10.1175/JCLI-D-13-
806   00248.1.
807 Sooraj, K. P., P. Terray, and M. Mujumdar, 2015: Global warming and the weakening of the
808   Asian summer monsoon circulation: assessments from the CMIP5 models. *Clim. Dyn.*, **45**,
809   233–252, https://doi.org/10.1007/s00382-014-2257-7.
810 Sperber, K. R., H. Annamalai, I.-S. Kang, A. Kitoh, A. Moise, A. Turner, B. Wang, and T. Zhou,
811   2013: The Asian summer monsoon: an intercomparison of CMIP5 vs. CMIP3 simulations
812   of the late 20th century. *Clim. Dyn.*, **41**, 2711–2744, https://doi.org/10.1007/s00382-012-
813   1607-6.
814 Swanson, K. L., 2008: Nonlocality of Atlantic tropical cyclone intensities. *Geochemistry,*
815   *Geophys. Geosystems*, **9**, n/a-n/a, https://doi.org/10.1029/2007GC001844.

816   Swart, N. C., and Coauthors, 2019: The Canadian Earth System Model version 5
817   (CanESM5.0.3). *Geosci. Model Dev.*, **12**, 4823–4873, https://doi.org/10.5194/gmd-12-4823-
818   2019.

819   Tian, B., and X. Dong, 2020: The Double- ITCZ Bias in CMIP3, CMIP5, and CMIP6 Models
820   Based on Annual Mean Precipitation. *Geophys. Res. Lett.*, **47**,
821   https://doi.org/10.1029/2020GL087232.

822   Vecchi, G. A., and B. J. Soden, 2007: Effect of remote sea surface temperature change on
823   tropical cyclone potential intensity. *Nature*, **450**, 1066–1070,
824   https://doi.org/10.1038/nature06423.

825   Vera, C., and G. Silvestri, 2009: Precipitation interannual variability in South America from the
826   WCRP-CMIP3 multi-model dataset. *Clim. Dyn.*, **32**, 1003–1014,
827   https://doi.org/10.1007/s00382-009-0534-7.

828   ——, ——, B. Liebmann, and P. González, 2006: Climate change scenarios for seasonal
829   precipitation in South America from IPCC-AR4 models. *Geophys. Res. Lett.*, **33**, L13707,
830   https://doi.org/10.1029/2006GL025759.

831   Voldoire, A., 2018: CMIP6 simulations of the CNRM-CERFACS based on CNRM-CM6-1
832   model for CMIP experiment historical. https://doi.org/10.22033/ESGF/CMIP6.4066.

833   Voldoire, A., and Coauthors, 2019: Evaluation of CMIP6 DECK Experiments With CNRM-
834   CM6- 1. *J. Adv. Model. Earth Syst.*, **11**, 2177–2213,
835   https://doi.org/10.1029/2019MS001683.

836   Volodin, E., and Coauthors, 2019: INM INM-CM5-0 model output prepared for CMIP6 CMIP
837   piControl. https://doi.org/10.22033/ESGF/CMIP6.5081.

838   Wang, B., and Coauthors, 2020a: Monsoons Climate Change Assessment. *Bull. Am. Meteorol.*
839   *Soc.*, **preprint**, https://doi.org/10.1175/BAMS-D-19-0335.1.

840   ——, C. Jin, and J. Liu, 2020b: Understanding Future Change of Global Monsoons Projected by
841   CMIP6 Models. *J. Clim.*, **33**, 6471–6489, https://doi.org/10.1175/JCLI-D-19-0993.1.

842   Wu, T., and Coauthors, 2019: The Beijing Climate Center Climate System Model (BCC-CSM):
843   the main progress from CMIP5 to CMIP6. *Geosci. Model Dev.*, **12**, 1573–1600,
844   https://doi.org/10.5194/gmd-12-1573-2019.

845   Xie, P., J. E. Janowiak, P. A. Arkin, R. Adler, A. Gruber, R. Ferraro, G. J. Huffman, and S.
846   Curtis, 2003: GPCP Pentad Precipitation Analyses: An Experimental Dataset Based on
847   Gauge Observations and Satellite Estimates. *J. Clim.*, **16**, 2197–2214,
848   https://doi.org/10.1175/2769.1.

849   Xin, X., T. Wu, J. Zhang, J. Yao, and Y. Fang, 2020: Comparison of CMIP6 and CMIP5
850   simulations of precipitation in China and the East Asian summer monsoon. *Int. J. Climatol.*,
851   joc.6590, https://doi.org/10.1002/joc.6590.

852   Yin, L., R. Fu, E. Shevliakova, and R. E. Dickinson, 2013: How well can CMIP5 simulate
853   precipitation and its controlling processes over tropical South America? *Clim. Dyn.*, **41**,
854   3127–3143, https://doi.org/10.1007/s00382-012-1582-y.

855   Yukimoto, S., and Coauthors, 2019: MRI MRI-ESM2.0 model output prepared for CMIP6
856   CMIP. https://doi.org/10.22033/ESGF/CMIP6.621.

857   Zhang, X., H. Liu, and M. Zhang, 2015: Double ITCZ in Coupled Ocean-Atmosphere Models:
858   From CMIP3 to CMIP5. *Geophys. Res. Lett.*, **42**, 8651–8659,
859   https://doi.org/10.1002/2015GL065973.

860   Zhang, Y., and S. Fueglistaler, 2020: How Tropical Convection Couples High Moist Static
861   Energy Over Land and Ocean. *Geophys. Res. Lett.*, **47**,

862   https://doi.org/10.1029/2019GL086387.
863
864
865
866
867
868
869
870
871
872
873
874
875
876
877
878
879
880
881
882
883
884
885
886
887
888
889
890
891
892
893
894
895
896
897
898
899
900
901

32

902 Table 1 - Model description and references. Simulations with available near-surface temperature and
903 humidity data for the calculation of near-surface Moist Static Energy are indicated with (*) for daily data
904 and (#) for monthly data.

Center/Model	Resolution (Lat x Lon)	Number of ensemble members			Key References
		Historical	SSP370	SSP585	
Beijing Climate Center (BCC) / BCC-CSM2-MR	1.125 x 1.125	3 (*,#)	1 (*,#)	1 (*,#)	(Wu et al. 2019)
Canadian Centre for Climate Modelling and Analysis (CCCma) / CanESM5	2.8125 x 2.8125	31 (*,#)	39 (*,#)	34 (*,#)	(Swart et al. 2019)
Centre National de Recherches Météorologiques (CNRM) - Centre Européen de Recherche et de Formation Avancée en Calcul Scientifique (CERFACS) / CNRM-CM6-1	1.40625 x 1.40625	13 (*,#)	1 (*,#)	1 (*,#)	(Voldoire 2018; Voldoire et al. 2019)
CNRM - CERFACS / CNRM-ESM2-1	1.40625 x 1.40625	5 (*,#)	1 (*,#)	1 (*,#)	(Séférian et al. 2016; Seferian 2018)
Institute for Numerical Mathematics (INM) / INM-CM5-0	1.5 x 2.0	1	1(*,#)	--	(Volodin et al. 2019)
Institut Pierre-Simon Laplace (IPSL) / IPSL-CM6A-LR	1.25 x 2.5	32 (#)	4 (#)	--	(Boucher et al. 2018)
Meteorological Research Institute (MRI) / MRI-ESM2-0	1.125 x 1.125	5 (*,#)	1 (#)	-	(Yukimoto et al. 2019)
National Center for Atmospheric Research (NCAR) / CESM2	0.9375 x 1.25	10 (*,#)	1	2(*,#)	(Danabasoglu 2019a)
NCAR / CESM2-WACCM	0.9375 x 1.25	3 (*,#)	1	--	(Danabasoglu 2019b)
Geophysical Fluid Dynamics Laboratory (GFDL) / GFDL-CM4	1.0 x 1.25	1 (*,#)	--	1 (*,#)	(Guo et al. 2018)
GFDL / GFDL-ESM4	1.0 x 1.25	1 (#)	1	1	(Krasting et al. 2018)
Nanjing University Information Science and Technology (NUIST) Earth System Model version 3 (NESM3) / NUIST-NESM3	1.875 x 1.875	1	--	1	(Cao and Wang 2019)

905
906
907
908
909

33

910

A) GPCP mean JJAS precipitation [mm/day]   **B) GPCP mean NDJF precipitation [mm/day]**

C) JJAS precipitation MME bias   **D) NDJF precipitaton MME bias**
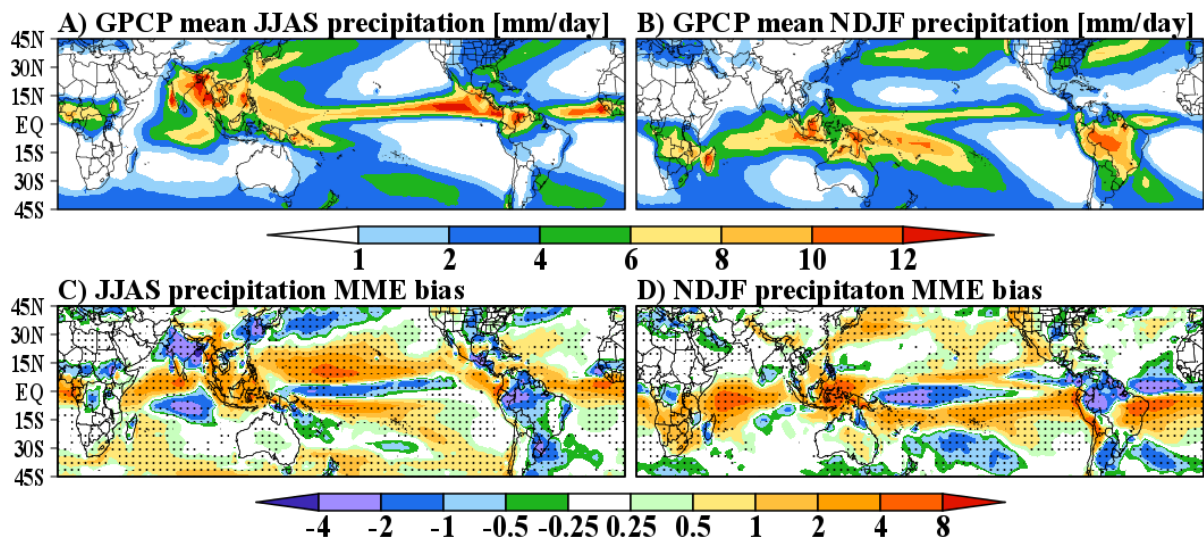
911
912
913 Figure 1 - Mean observed (GPCP) seasonal precipitation [mm.d⁻¹] during A) June through September and
914 B) November through February; MME bias of seasonal precipitation in historical runs during C) June
915 through September and D) November through February. The period considered is from 1981 to 2010. The
916 stippling represents grid points where at least 80% of the models have the same bias sign.

917
918
919
920
921
922
923
924
925
926
927
928
929
930
931
932
933
934
935
936
937
938
939
940
941
942
943
944

945

A) Percentage of annual rainfall during the wet season (TRMM)

B) Percentage of annual rainfall during the wet season (Historical)
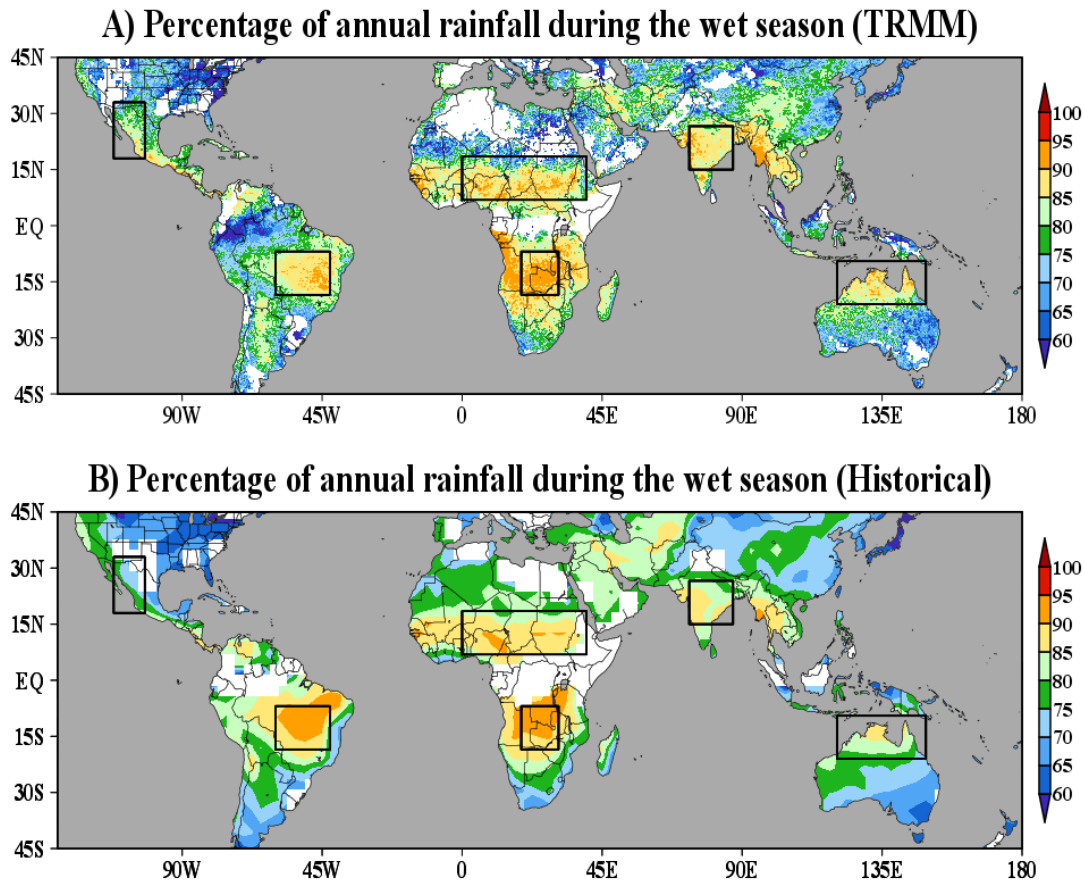
946
947 Figure 2 - Median percentage of annual precipitation that falls during the wet season for A) precipitation
948 from TRMM and B) precipitation from historical runs (considering only models with available SSP370
949 simulations). The boxes in frame A indicate some of the regions of interest used for further analysis.
950 Domains: North America [18°N-33°N;248°E-258°E]; South America [18.5°S-7°S;300°E-318°E]; Sahel
951 [7°N-18.5°N;0-40°E], Southern Africa [18.5°S-7°S;19.5°E-31°E]; India [15°N-27°N;73°E-87°E]; and
952 Northern Australia [21°S-9.5°S;120.5°E-149°E]. Masked regions (in white) are regions with multiple wet
953 season or regions without a clear wet season (see Sec. 2 and Bombardi et al. 2019).
954
955
956
957
958
959
960
961
962
963
964
965

35

966
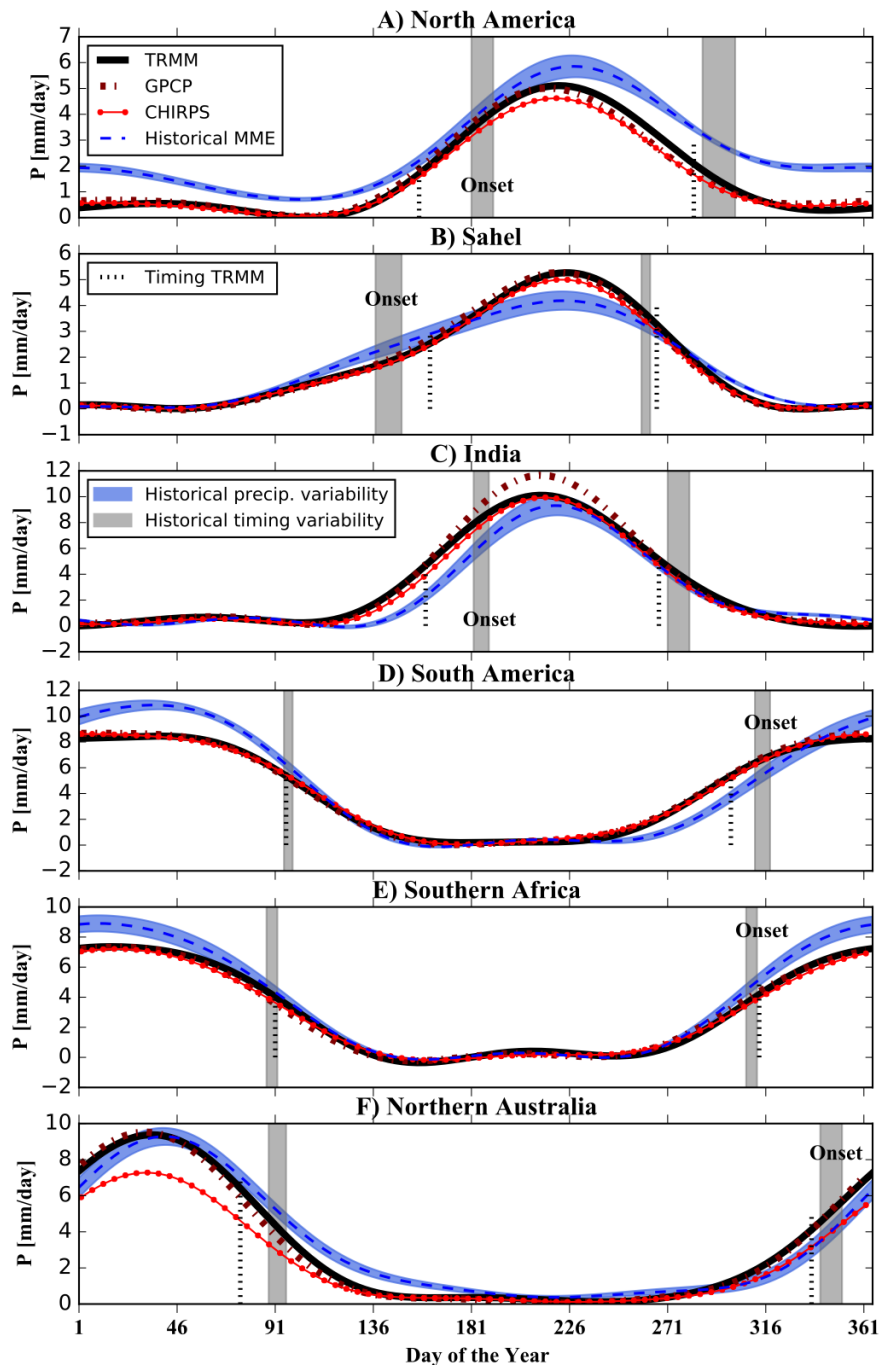
967
968 Figure 3 - Smoothed mean annual cycle of precipitation for observations and simulations spatially
969 averaged over the regions shown in Fig. 2. Only values over land are included in the analysis. The figure
970 includes the mean annual cycle of precipitation from GPCP, CHIRPS, and TRMM. For models with more
971 than one integration, we first calculate the ensemble mean before calculating the MME mean to guarantee
972 that each model has the same weight on the MME mean. The shading represents the MME spread as the
973 standard error of the mean above and below the MME mean of historical runs. The vertical dashed line
974 represents the median onset and demise dates for TRMM. The vertical shading indicates the MME mean
975 of the median onset and demise dates of the full set of historical runs (12 models), plus and minus the
976 standard error of the mean. The period considered is from 1981 to 2010. The mean annual cycle of
977 precipitation in all datasets was smoothed using the first 3 harmonics.

36

978
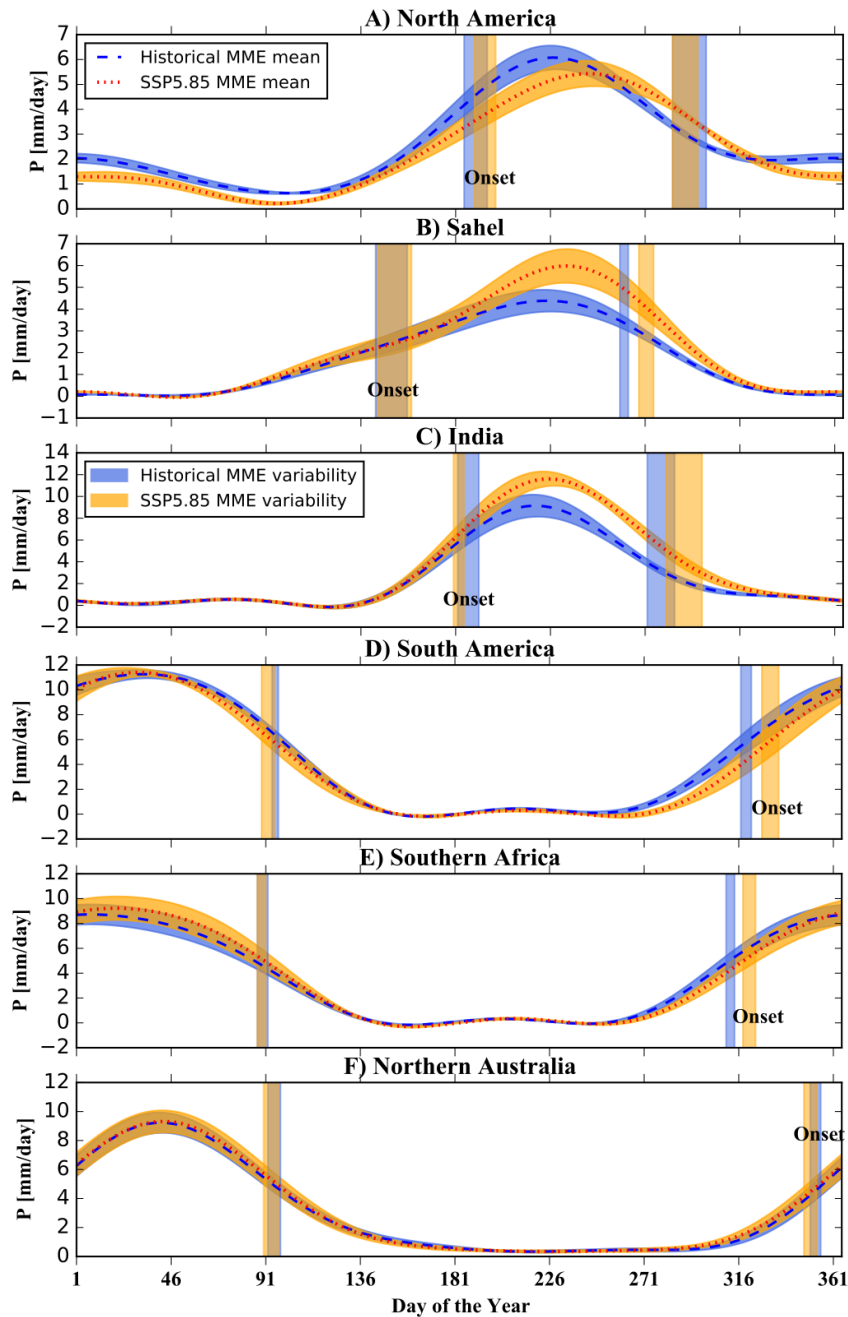
979
980 Figure 4 - Smoothed mean annual cycle of precipitation for historical and SSP5.85 simulations spatially
981 averaged over the regions shown in Fig. 2. Only values over land are included in the analysis. Only
982 models with available simulations for both scenarios were considered (8 models). The dashed line
983 represents the MME mean of historical runs and the dotted line represents the MME mean of SSP5.85
984 runs. The shading represents the MME spread as one standard error of the mean above and below the
985 MME mean. The vertical shading indicates the MME mean of the median onset and demise dates of the
986 full set of historical runs (8 models), plus and minus the standard error of the mean.. The period
987 considered is from 1981 to 2010 for historical runs and 2071 to 2100 for SSP5.85 runs. The mean annual
988 cycle of precipitation was smoothed using the first 3 harmonics. Note that the shading has 70% opacity in
989 order to allow comparison between experiments. The overlapping range between historical and SSP5.85
990 runs is denoted by the intermediate orange-blue hue.
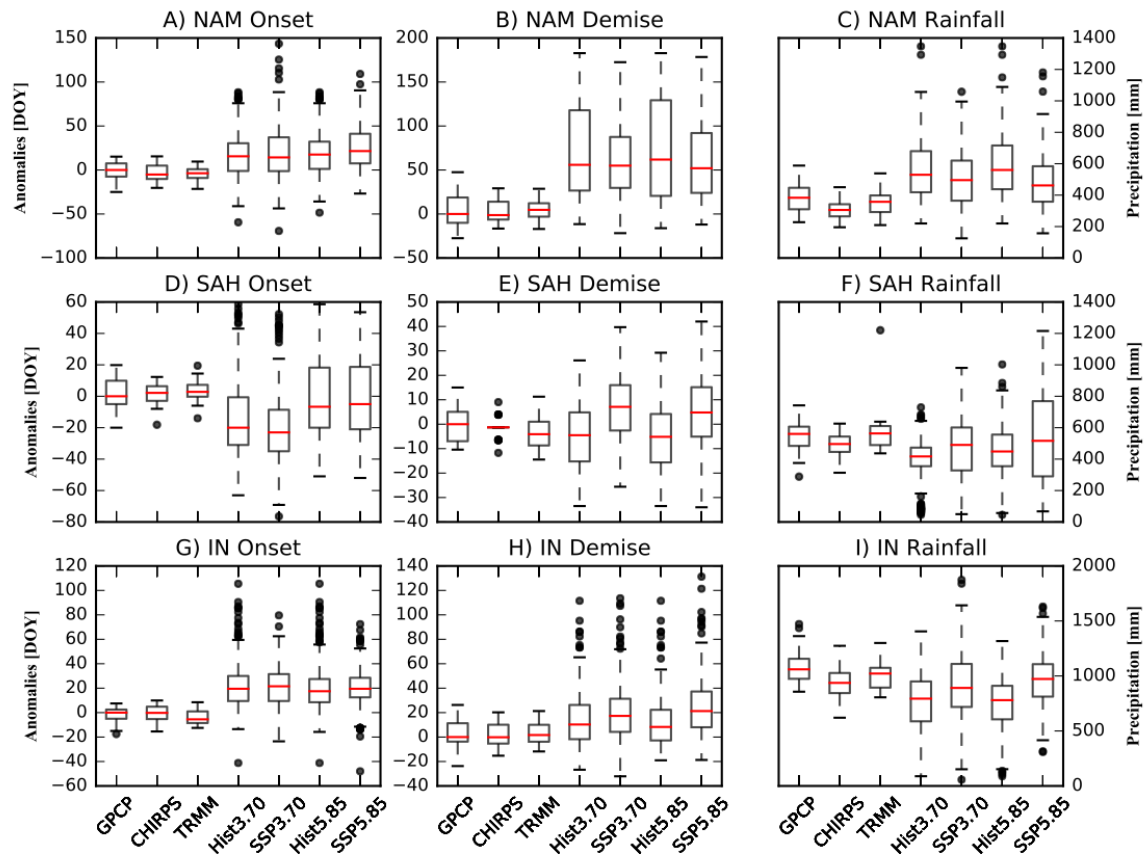
37

994
995 Figure 5 – Boxplot of the interannual variability of the characteristics of the rainy season. Horizontally,
996 the frames show results for the North American Monsoon (NAM, top), Sahel (SAH, middle), and Indian
997 Monsoon (IM, bottom) domains. Vertically, the frames show onset (left), demise (middle), and wet
998 season rainfall (right). Results are shown for three different precipitation observations as well as historical
999 and scenario runs. Since there are different sets of models for scenario SSP3.70 and SSP5.85, the
1000 historical runs are showed twice, matching the models available in each future scenario. Thus, Hist3.70
1001 represent historical runs for the same models in the SSP3.70 scenario. Likewise, Hist5.85 represent
1002 historical runs for the models in the SSP5.85 scenario. The analysis was carried out by first taking the
1003 median value for each year for each domain and then generating the boxplots. For this analysis, only one
1004 member from each model was included to avoid biases toward models with multiple realizations. Each
1005 model contributes one value (median over the domain) per year for each year of simulation during a 35
1006 year period. The box extends from the lower to upper quartile values of the data, with a line at the
1007 median. Whiskers are defined as 1.5 times que interquartile ($75^{th} - 25^{th}$ percentiles) range above or below
1008 the box. Fliers are points beyond the whiskers.
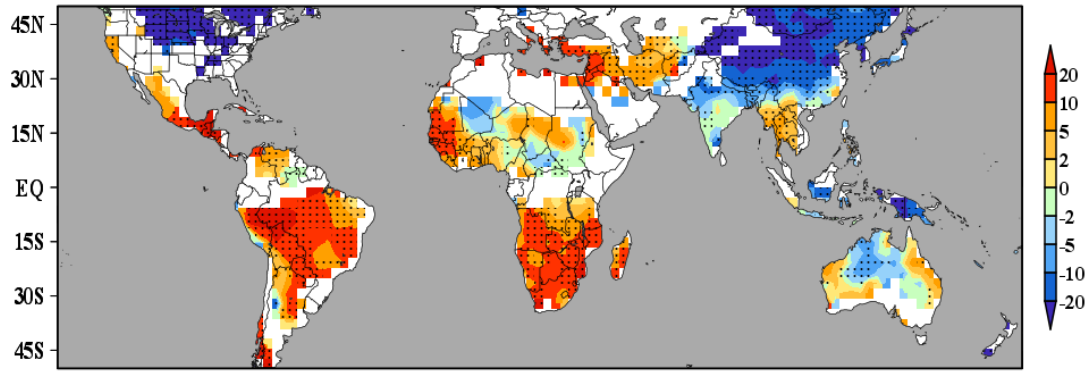1009
1010
1011

1012
1013
1014
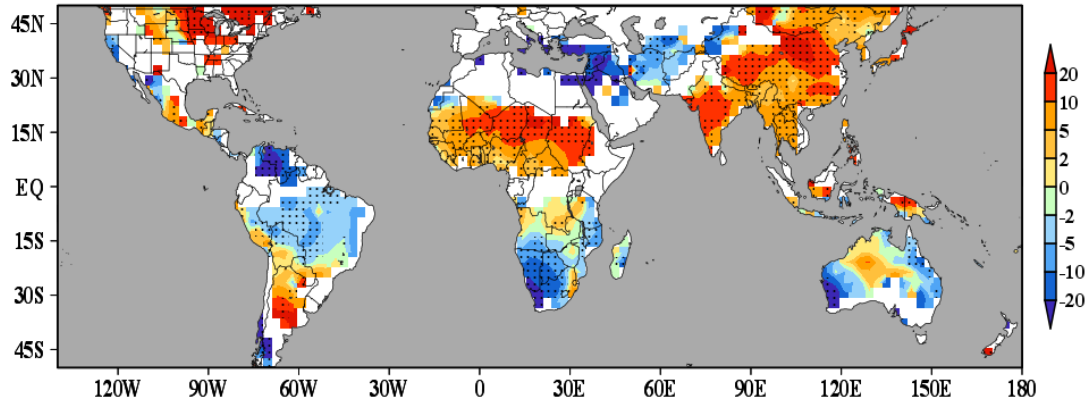1015
1016
1017
1018

1019
1020 Figure 6 – As in Fig.5, but for the South American Monsoon (SAM, top); Southern Africa (SAF, middle),
1021 and Northern Australian Monsoon (AUM, bottom).
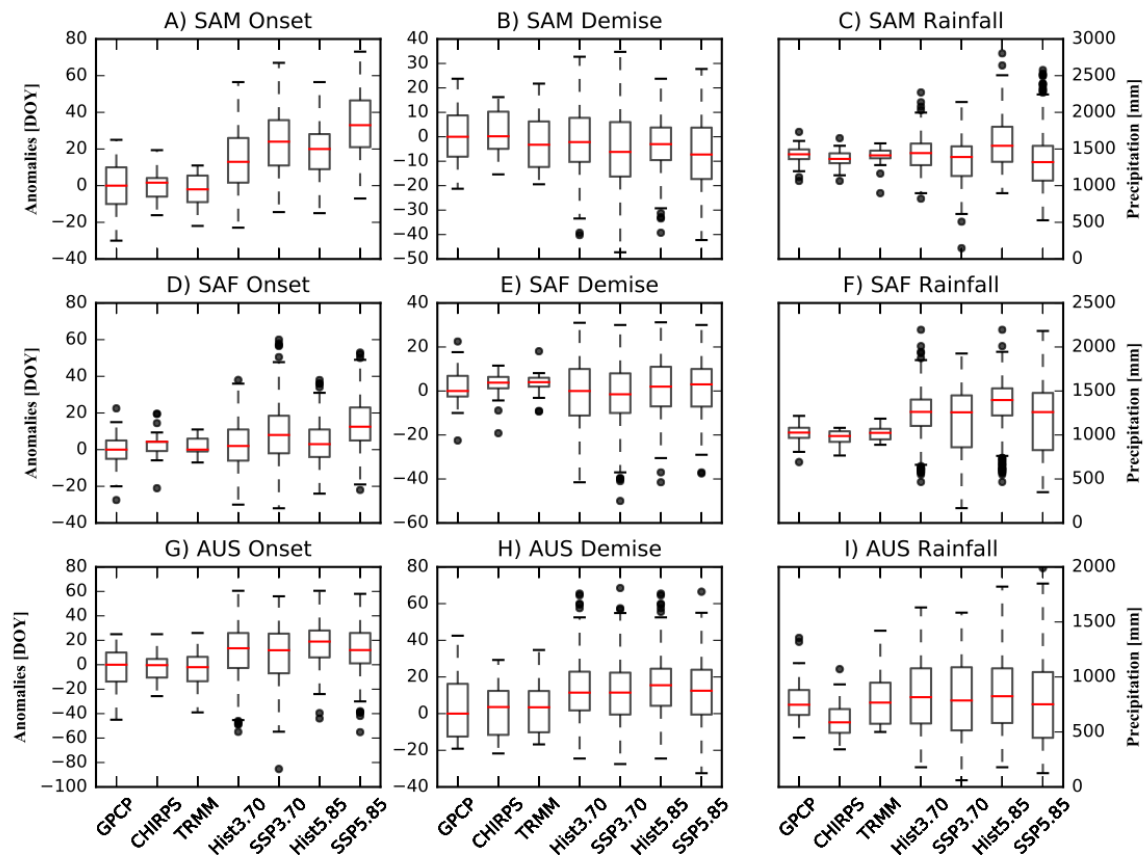
1022
1023
1024
1025
1026
1027
1028
1029
1030
1031
1032

39

1033

A) Wet season onset difference (SSP5.85 - Hist)

B) Wet season demise difference (SSP5.85 - Hist)
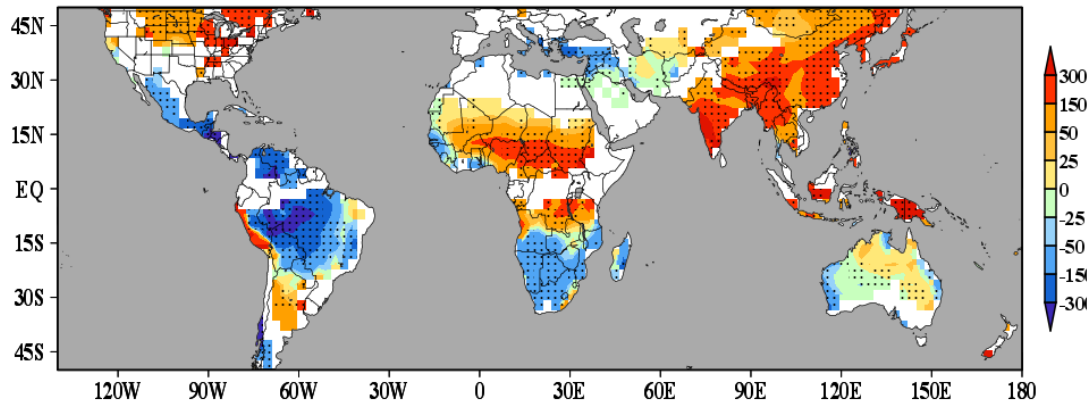

1034

C) Wet season precipitation difference (SSP5.85 - Hist)

1035
1036 Figure 7 - Difference between future scenario SSP5.85 and historical runs for A) median onset date, B)
1037 median demise date, and C) median total precipitation during the wet season. Stippling indicates regions
1038 where at least 7 out of 10 models show the same difference sign. Masked regions (in white) are regions
1039 with multiple wet season or regions without a clear wet season (see Sec. 2 and Bombardi et al. 2019).
1040
1041
1042
1043
1044

40

1045

A) ERA5 mean 2m-MSE (JJAS)

B) ERA5 mean 2m-MSE (NDJF)
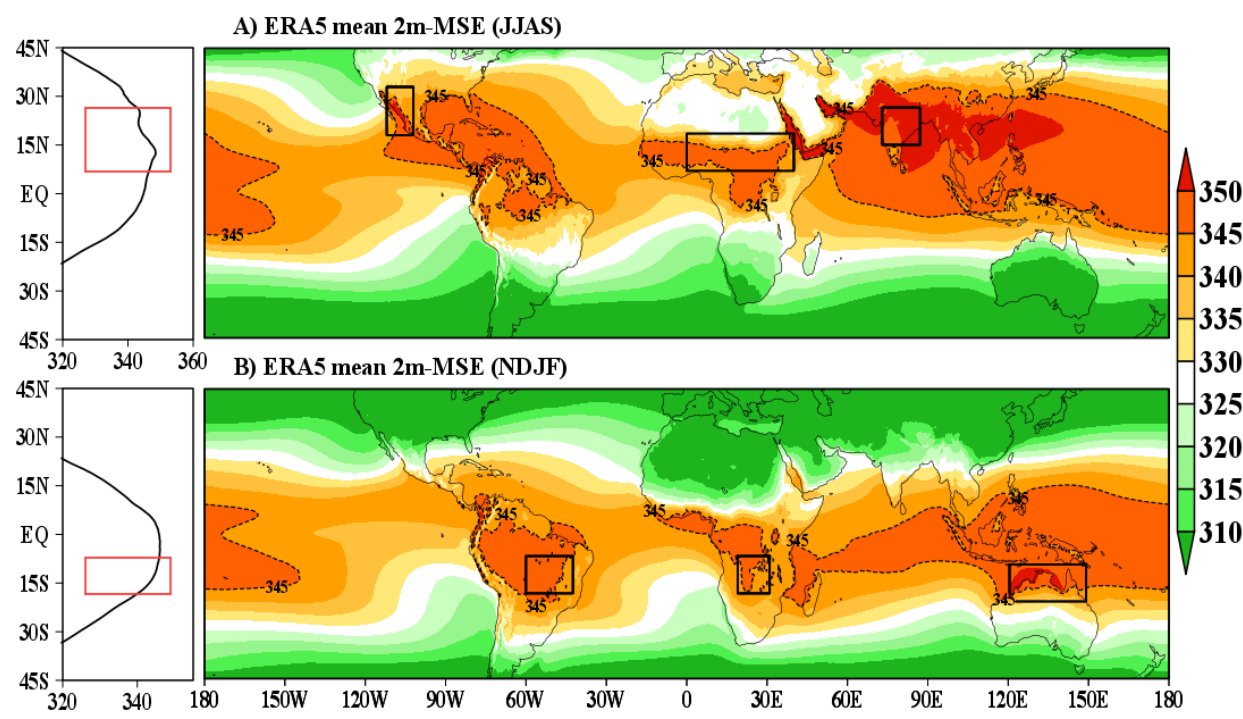
1046
1047 Figure 8 – Seasonal spatial pattern and zonal mean of observed (ERA5) near-surface MSE [KJ.kg^{-1}]
1048 during A) June through September and B) November through February. Dashed contours show the value
1049 of 345 KJ.kg^{-1}, highlighting that the maximum near-surface MSE values occur over monsoonal regions.
1050 The boxes show the monsoon domains of interest. In A), the box in the zonal mean frame comprises the
1051 domain of both India and Sahel. In B), the box in the zonal mean frame comprises the domains of both
1052 South America and Southern Africa. The period considered is from 1981 to 2010.
1053
1054
1055
1056
1057
1058
1059
1060
1061
1062
1063
1064
1065
1066
1067
1068
1069
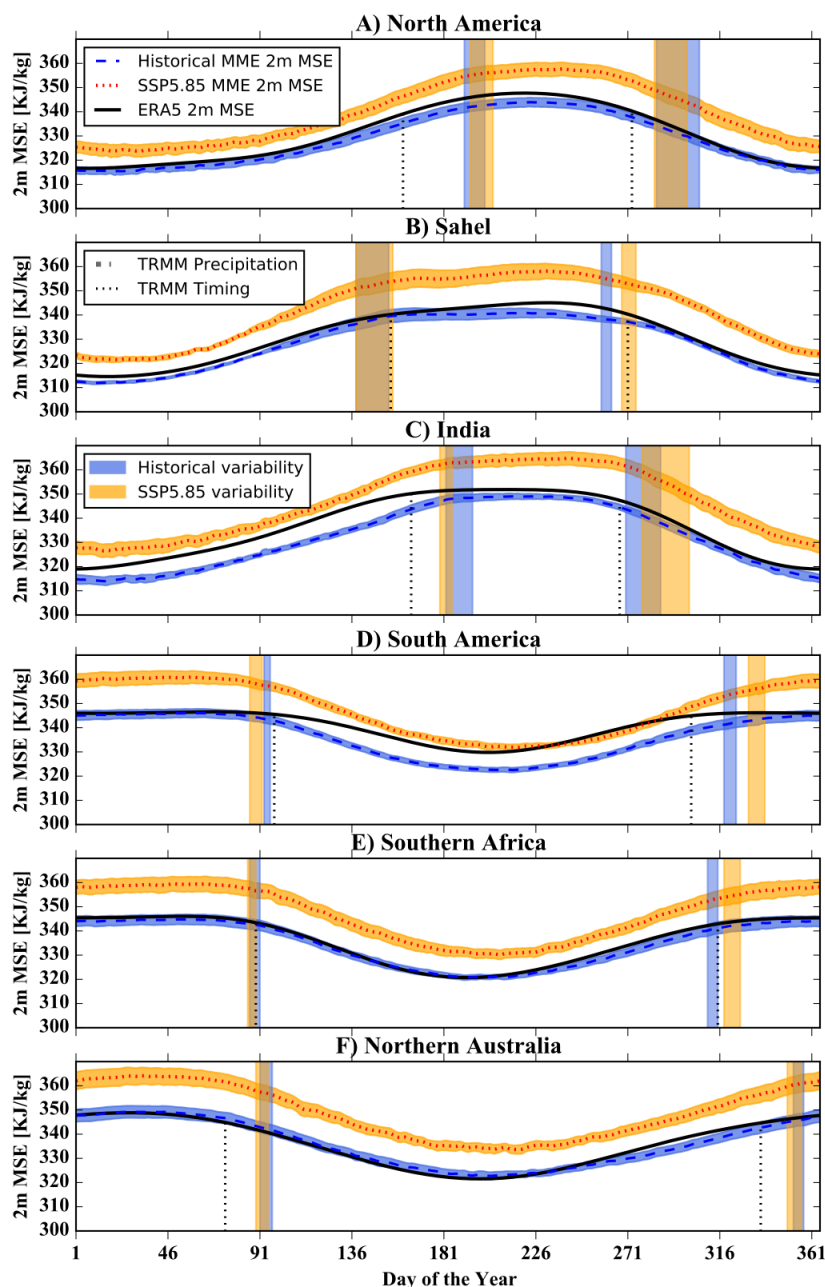1070
1071
1072

41

1073

1074
1075 Figure 9 - Smoothed mean annual cycle of near-surface MSE for observations (thick solid black line,
1076 ERA5) as well as historical and SSP5.85 simulations, spatially averaged over the regions shown in Fig. 2.
1077 Only values over land are included in the analysis. Only models with available simulations for both
1078 scenarios were considered (8 models). The shading represents the MME spread as one standard error of
1079 the mean above and below the MME mean. The vertical shading indicates the MME mean of the median
1080 onset and demise dates of the full set of historical runs (8 models), plus and minus the standard error of
1081 the mean. The vertical dashed line shows the median onset and demise dates from TRMM. The thick
1082 dashed line shows the observed mean annual cycle of precipitation from TRMM. The period considered is
1083 from 1981 to 2010 for observations and historical runs and 2071 to 2100 for SSP5.85 runs. The mean
1084 annual cycle was smoothed using the first 3 harmonics. Note that the shading has 70% opacity in order to
1085 allow comparison between experiments. The overlapping range between historical and SSP5.85 runs is
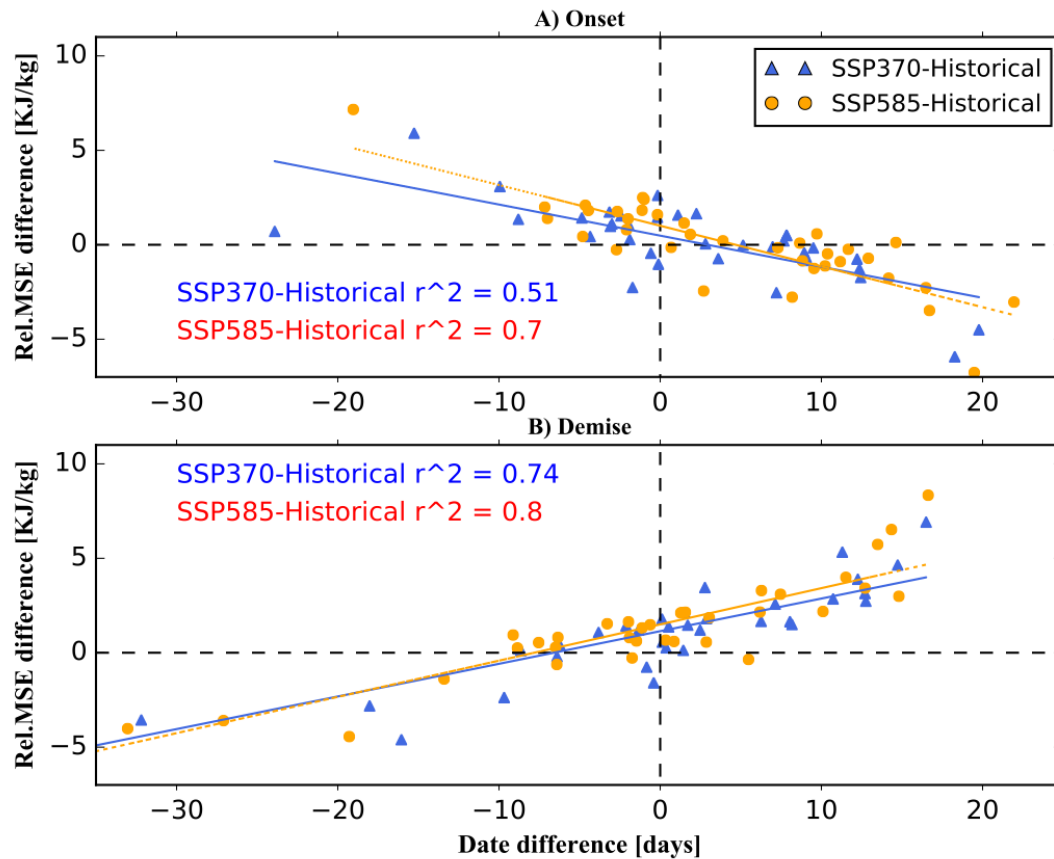1086 denoted by the intermediate orange-blue hue.

42

1087
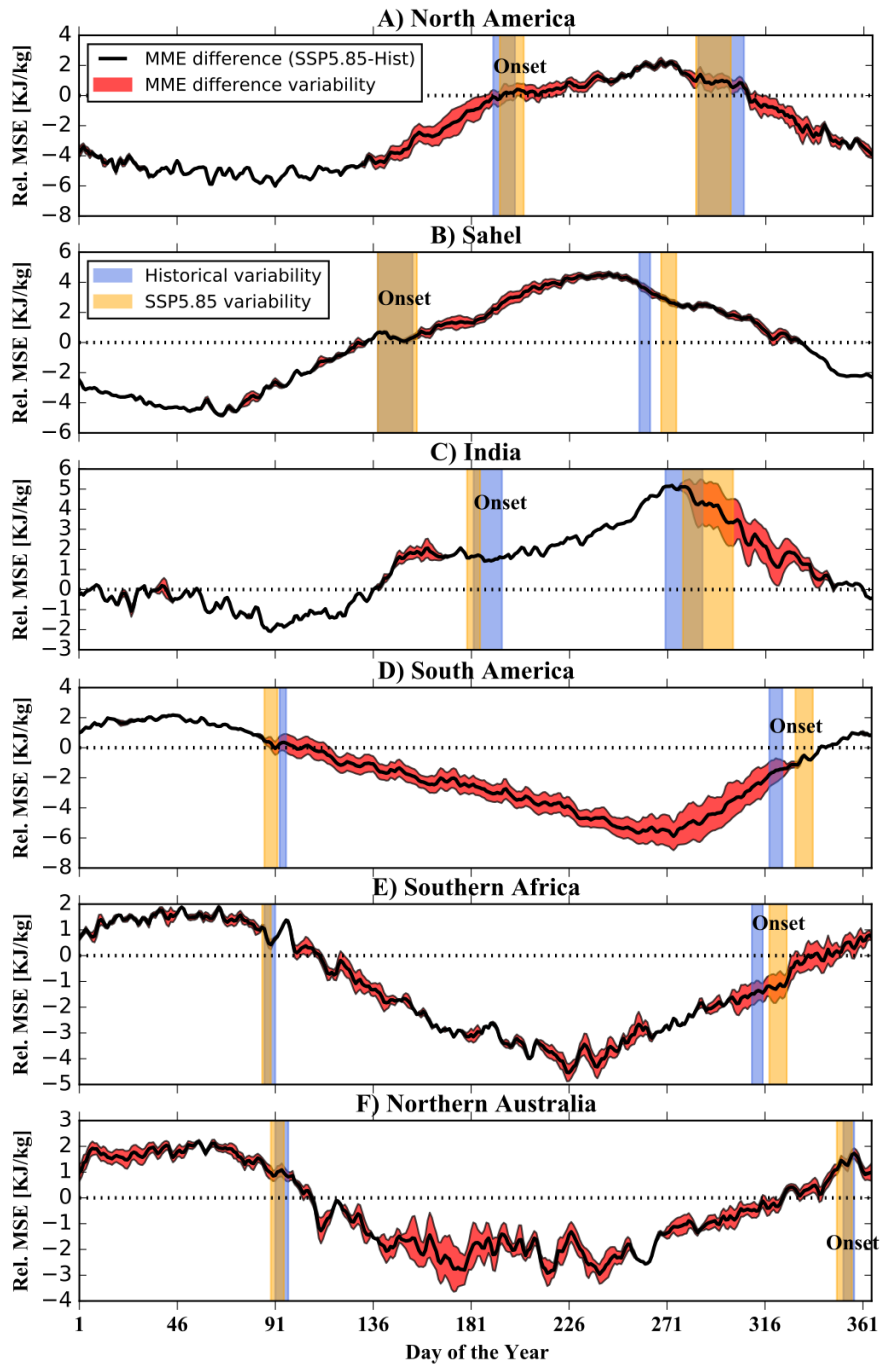
1089
1090 Figure 10 - Difference between SSP5.85 and historical mean annual cycle of relative surface MSE.
1091 Values are spatially averaged over the regions shown in Fig. 2. Only values over land are included in the
1092 analysis. Only models with available simulations for both scenarios were considered (6 models). For
1093 models with more than one integration, we first calculate the ensemble mean before calculating the MME
1094 mean to guarantee that each model has the same weight on the MME. The shading represents the spread
1095 in simulations as one standard error of the mean above and below the MME mean. The period considered
1096 for historical runs is from 1981 to 2010 and the period considered for SSP5.85 runs is from 2071 to 2100.
1097 Vertical shadings show the MME variability (mean plus and minus one standard error of the mean across
1098 all models) for onset and demise dates for each experiment.

43

1099
1100
1101
1102
1103

A) Onset

B) Demise

1104
1105 Figure 11 – Scatterplot of the difference (scenario minus historical runs) in relative near-surface
1106 MSE as a function of A) onset date difference and B) demise date differences. The plots include
1107 values from all core monsoon regions (Fig. 2). Each value of onset, demise, or relative near-
1108 surface MSE is calculated as the spatial average over each core monsoon region. Relative near-
1109 surface MSE averages are taken over the period the mean onset (or demise) month for each
1110 member of each model. The figure also includes the best linear fit for each scenario. All r^2 are
1111 statistically significant at 5% level.

1112
1113
1114
1115
1116
1117
1118
1119
1120

1121

1122
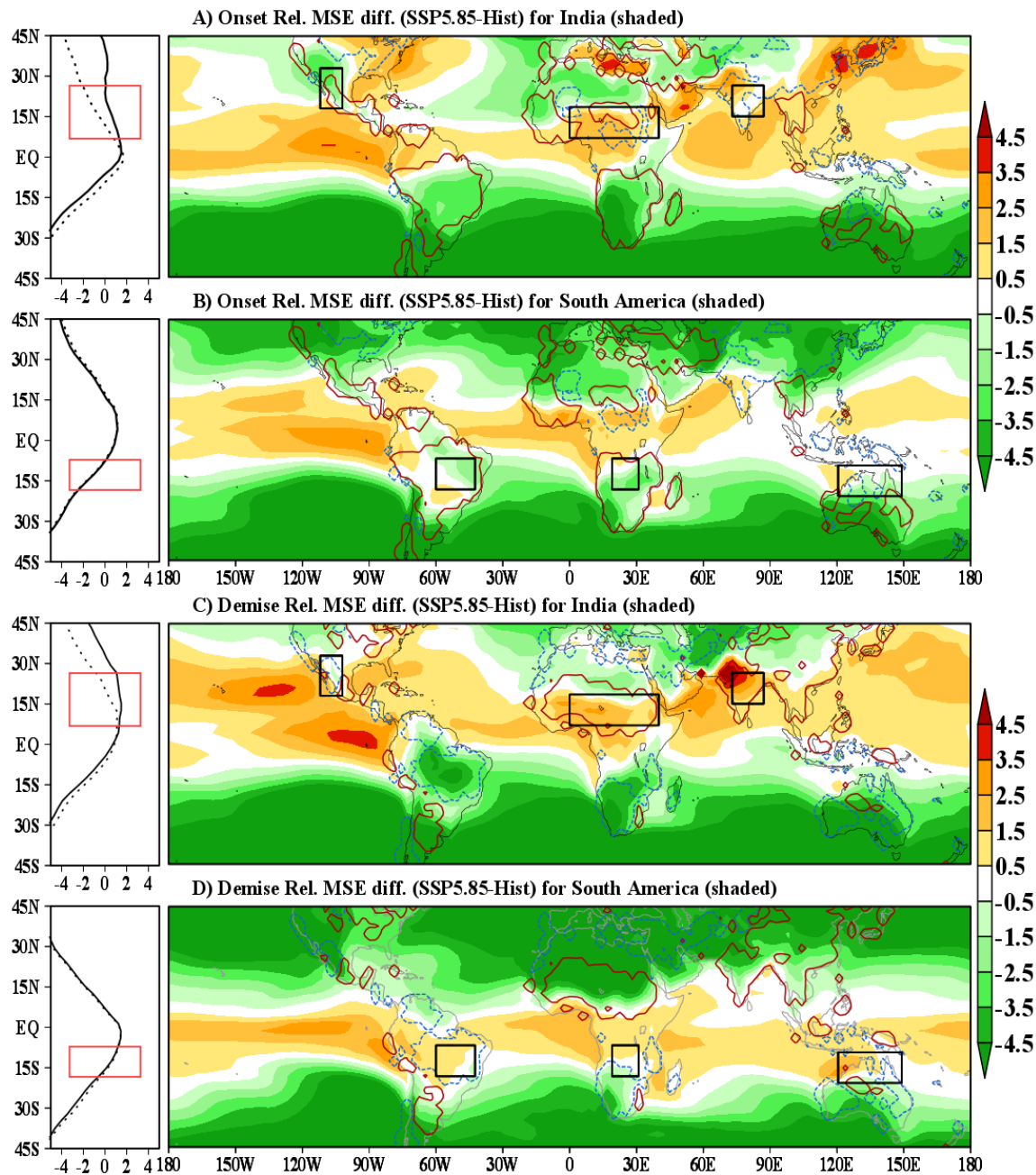
1123
1124 Figure 12 – Spatial pattern and zonal mean of MME average of relative near-surface MSE differences
1125 (SSP5.85 – Historical) during the ***onset*** over A) India (shading and zonal mean solid line) and the Sahel
1126 (zonal mean dashed line) and B) South America (shading and zonal mean solid line) and southern Africa
1127 (zonal mean dashed line). Spatial pattern and zonal mean of MME average of relative near-surface MSE
1128 differences (SSP5.85 – Historical) during the ***demise*** over C) India (shading and zonal mean solid line)
1129 and the Sahel (zonal mean dashed line) and D) South America (shading and zonal mean solid line) and
1130 southern Africa (zonal mean dashed line). Averages are calculated for the median onset (or demise)
1131 month in the historical run of each model. Solid red contours indicate positive changes of 3 days in onset
1132 dates in (A) and (B) and demise dates in (C) and (D). Dashed blue contours indicate negative changes of 3
1133 days in onset dates in (A) and (B) and demise dates in (C) and (D). Zonal means are calculated over the
1134 whole tropics. Only models with available simulations for both scenarios were considered (6 models).

45